

Bayesian formalism for distinguishing kilonova from neutron star-blackhole and binary neutron star mergers

Project Report PH 595

Yugesh Bhoge (23N0278)

Guided by: Professor Rahul Kashyap



Department of Physics
Indian Institute of Technology Bombay, Mumbai

December 11, 2025

Abstract

GW170817, the first detection of a multimessenger phenomenon, opens doors to new development in the field of astrophysics, enabling comprehensive exploration of compact binary mergers and their associated electromagnetic events, such as kilonovae. This report introduces a Bayesian technique to distinguish kilonovae arising from mergers of binary neutron stars (BNS) and neutron star-black hole (NSBH) systems. The analysis integrates gravitational wave parameter estimation through Bilby and MOSFiT, with light curve modelling from the Arnett-Chatzopoulos-Villar (ACV) model. We present a framework that enables the prediction, detection, and identification of the merger type solely from the kilonova light curve. The analysis focuses first on the observable parameters detected through interferometers such as M_{Chirp} , q and $\tilde{\Lambda}$, and subsequently on the intrinsic Compact Binary Coalescence (CBC) parameters such as M_1 , M_2 , Λ_1 and Λ_2 in case of BNS mergers and M_1 , M_2 , χ_1 and Λ_2 in case of NSBH systems. We have used various fitting formulae to convert ejecta properties like M_{ej} , v_{ej} , etc., estimated using a simulated population of light curves, into CBC-based parameters, thereby lifting the degeneracies in gravitational wave as well as in electromagnetic observations.

Keywords: *multi-messenger astrophysics, Gravitational wave, kilonova, Bayesian parameter estimation, lightcurve modelling, binary neutron star, neutron star black hole*

Acknowledgment

I like to convey my profound appreciation to my project supervisor, Professor Rahul Kashyap, for his indispensable direction and assistance during this research. I also thank my peer Mr. Vasudev Dubey for helping with code-related issues. I would also like to thank Mr. Ish Gupta (Penn State) for lending us important insights into the data and the coding part of the project. I would also like to thank IIT Bombay's Spacetime cluster team for lending us the supercomputer resources, which were and still are crucial for the runs. Lastly, I would also like to thank every faculty at the Indian Institute of Technology Bombay for their support and feedback.

List of Figures

3.1	<i>Plot between κ and Y_e showcasing decrease of opacity with increase in electron fraction</i>	22
4.1	<i>A Sample 8 parameter NSBH Corner plot generated using IMRPhenomNSBH waveform approximant with nested sampler dynesty was used with $q = 0.25$</i>	25
4.2	<i>Comparisons between relative errors in 4 parameters among 100 NSBH runs for 3 detectors using IMRPhenomTidalv2 waveform approximant for APR4 and SLy EOS</i>	26
4.3	<i>Corner plots of best runs for NSBH for ECC detectors using IMRPhenomTidalv2 waveform approximant for APR4 and SLy EOS</i>	27
4.4	<i>Subplots of relative errors versus injected parameters for ECC detector with APR4 EoS</i>	28
4.5	<i>Subplots of relative errors versus injected parameters for ECC detector with SLy EoS</i>	29
4.6	<i>Corner plots of best runs for BNS for ECC detectors using IMRPhenomTidalv2 waveform approximant for APR4, DD2 and SLy EOS</i>	30
4.7	<i>Comparisons between relative errors in 4 parameters among 100 BNS runs for 3 detectors using IMRPhenomTidalv2 waveform approximant for APR4, DD2 and SLy EOS</i>	31
4.8	<i>Filter transmission as function of wavelength</i>	32
4.9	<i>Comparison between Apparent Magnitude bandwise lightcurves using realistic and ideal filters for NSBH system</i>	33
4.10	<i>Comparison between bandwise lightcurves using realistic and ideal filters</i>	33
4.11	<i>Corner plot for parameter estimation using MOSFiT’s NSBH model</i>	34
4.12	<i>A bullet plot showing comparison between injected and recovered parameters for NSBH system</i>	35
4.13	<i>Comparison between Apparent Magnitude bandwise lightcurves using realistic and ideal filters for BNS system</i>	35
4.14	<i>Comparison between bandwise lightcurves using realistic and ideal filters</i>	36
4.15	<i>A bullet plot showing comparison between injected and recovered parameters for BNS system</i>	37
4.16	<i>Corner plot for parameter estimation using MOSFiT’s BNS model</i>	38

List of Tables

4.1	<i>Injected parameters and their values for sample NSBH run from figure 4.1</i>	26
4.2	Injected parameter	34
4.3	Injected parameter	36

Contents

Abstract	i
Acknowledgment	ii
1 Introduction	2
1.1 Introduction to Kilonovae	2
1.1.1 History of Kilonovae Observations	2
1.1.2 Mechanism of Kilonovae	3
1.1.3 Arnett’s model to predict Lightcurve [1], [2]	4
1.1.4 Modification to Arnett’s model for Kilonovae inclusion:	6
1.1.5 Kilonovae from BNS vs. NSBH Mergers	8
1.2 Introduction to Bayesian Inference in MOSFiT pipeline	9
1.2.1 The Bayesian Framework	9
1.2.2 From Parameters to Synthetic Photometry	10
1.2.3 Choice of Likelihood	10
1.2.4 Specification of Priors	11
1.2.5 Posterior Evaluation	11
1.2.6 Sampling Strategy	11
1.2.7 Evidence and Model Comparison	11
1.2.8 Outputs	11
1.3 Introduction to Bayesian Inference in Gravitational Wave Physics:	12
1.3.1 Introduction	12
1.3.2 The Role of Bayesian Inference in Gravitational-Wave Physics	12
1.3.3 Key Concepts of Bayesian Inference	13
1.3.4 Parameter Estimation and Model Selection	13
1.3.5 Computational Methods for Bayesian Inference	14
2 Motivation	16
3 Methodology	17
3.1 Flowchart:	17
3.1.1 Kilonova Inference	18
3.1.2 GW Inference:	19
3.2 Calculating BNS Lightcurve:	19
3.2.1 General Structure	19
3.2.2 Dynamical Ejecta	19
3.2.3 Disk Wind Ejecta	20
3.2.4 Ejecta Velocity Calculation	20
3.2.5 Light Curve Heating Rate	20

3.2.6	Diffusion and Bolometric Luminosity	21
3.2.7	Photospheric Emission	22
3.2.8	Blackbody Emission and AB Magnitude	23
3.2.9	Gravitational Wave Related Quantities	23
3.3	Calculating NSBH Lightcurve:	23
3.3.1	ISCO Radius	23
3.3.2	Remnant Mass	24
3.3.3	Dynamical Ejecta Mass	24
3.3.4	Unbound Disk Mass	24
3.3.5	Ejecta Velocity	24
3.4	Calculating Bandwise Lightcurve:	24
4	Progress and Results	25
4.1	NSBH results	25
4.2	BNS results	30
4.3	Calculated Lightcurves	32
4.3.1	Filters used:	32
4.3.2	For NSBH system:	33
4.3.3	For BNS system:	35
5	Future Work	39
6	Conclusion	40

Chapter 1

Introduction

The first gravitational wave observation was made on September 14, 2015, which marked the beginning of the new era of gravitational wave physics[11]. The interesting part of this discovery was that the binary system was a Black Hole merger **GW150914** with individual masses of $36M_{\odot}$ and $29M_{\odot}$. This marked a big achievement in the context of the theory of general relativity. Previously, all astronomical observations were conducted using electromagnetic waves; nevertheless, this has introduced a novel avenue for observing the universe. Following this, numerous further BBH mergers were found. The next breakthrough came when the first Binary Neutron Star (BNS) merger was detected on August 17th, 2017. This event which was named **GW170817**, was very special as we not only detected its gravitational waves signal, but also detected a kilonova(**AT2017gfo**) and short gamma-ray bursts(**GRB 170817A**). These multimessenger observations proved that short GRBs originate from neutron star mergers. The detection of these BNS signals was fortunate because, until the third observation cycle, only one other BNS merger was discovered following GW170817[11].

1.1 Introduction to Kilonovae

Kilonovae are brief astronomical phenomena that occur when compact objects like neutron stars (NS) merge. They are fueled by the radioactive decay of heavy elements, usually lanthanides and actinides. The process responsible for producing these heavy elements is the rapid neutron-capture process (*r*-process) during and after NS mergers. Kilonovae emit across a broad range of electromagnetic spectrum, including optical, infrared, and X-ray, making them key objects of study in multi-messenger astronomy[16]. Kilonovae gained wide recognition after the detection of gravitational waves (GW170817) from the binary neutron star (BNS) merger in 2017, followed by detection of its electromagnetic counterpart, AT 2017gfo. This event confirmed that neutron star mergers are sites of short gamma-ray bursts and *r*-process nucleosynthesis, which creates elements heavier than iron such as gold and platinum [24].

1.1.1 History of Kilonovae Observations

The concept of a kilonova was first proposed by [22] to describe an optical transient that was the byproduct of the radioactive decay of heavy elements produced in the merger of two neutron stars. Although these events were initially theorized, the first observed kilonova was detected following the short gamma-ray burst GRB 130603B. This event

proved that optical and infrared emission may originate from neutron-rich ejecta in compact object mergers [29, 6].

The detection of GW170817 and its associated kilonova AT 2017gfo [10] marked the beginning of the era of multi-messenger astrophysics, where gravitational waves and electromagnetic signals from the same event were observed. This event confirmed that BNS mergers are significant sources of heavy elements in the universe.

1.1.2 Mechanism of Kilonovae

Kilonovae result from the complex interplay of various astrophysical processes, predominantly powered by the radioactive decay of neutron-rich nuclei formed during r-process nucleosynthesis in the ejecta of neutron star mergers.

R-process Nucleosynthesis

The r-process, or rapid neutron-capture process, is a nucleosynthesis pathway that enables the formation of heavy elements (beyond iron) under conditions of extreme neutron flux. During events like neutron star mergers, a significant amount of neutron-rich material is ejected. In this environment, nuclei capture neutrons at a rate faster than their beta decay, building up heavy, neutron-rich isotopes. The process proceeds along a path close to the neutron drip line, forming nuclei that are highly unstable and far from the line of stability. Once the neutron supply diminishes, these nuclei are left to decay into more stable forms through subsequent radioactive decay processes.

Beta Decay Heating

The neutron-rich nuclei produced during r-process nucleosynthesis are unstable and undergo beta decay to achieve stability. In each beta decay, a neutron is converted into a proton, releasing an electron and an antineutrino. While neutrinos typically escape without interacting with the surrounding material, the emitted electrons contribute to heating the ejecta. This heating process releases energy over time and powers the electromagnetic emission observed as a kilonova. The beta decay heating plays a critical role in sustaining the luminosity over days to weeks following the merger event.

Heating Rate

The heating rate of the ejecta is a crucial factor that influences the light curve of a kilonova. It can be approximated as a function of time, with the rate depending on properties such as the mean life of the decaying nuclei and the energy released per decay. The heating rate per unit mass, $Q(t)$, typically follows a power-law decay due to the continuous series of beta decays occurring over different timescales. This rate ensures that the energy deposition initially sustains the bright emission and gradually diminishes as the nuclei decay towards more stable states.

Thermalization Efficiency

While beta decay releases substantial energy, not all of it is converted into observable light. The fraction of energy that contributes to the thermal energy of the ejecta, known as thermalization efficiency, depends on several factors, including particle interactions

within the ejecta. Processes such as Compton scattering, photoelectric absorption, and pair production affect how much of the decay energy is deposited as heat. Compton scattering involves photons transferring energy to electrons, while photoelectric absorption dominates for photon energies near the ionization energy of atoms. Pair production can occur for very high-energy photons. The efficiency of these processes determines how effectively the kinetic energy of the decay products is thermalized and radiated as visible light, shaping the observed kilonova light curve [17, 18].

1.1.3 Arnett's model to predict Lightcurve [1], [2]

In 1980 and 1982 W. David Arnett proposed a framework to understand radioactively powered lightcurve analytically. Although his model was based on type Ia and type II supernovae later on many people expand/modify this model to fit for kilonovae using various numerical simulation to obtain the best fit. Arnett's model was based on simple assumptions,

- **Homologous expansion:** The expansion of Supernovae ejecta is assumed to be homologous (i.e. Hubble like expansion), where $v_i \propto r_i$, where v_i is velocity of i^{th} particle at distance r_i from the centre.
- **Radiation Dominated Ejecta:** Thermal energy E is dominated by radiation ($E \sim aT^4V$) and the equation of state is $P = \frac{E}{3V}$.
- **Diffusion approximation for photon transport:** Under effectively constant κ (opacity) photon are diffusing out of ejecta with luminosity relation as $L \propto \frac{\partial(aT^4)}{\partial r}$. This diffusion approximation will lead us to calculate the flux.
- **Spherical symmetry:** The ejecta is assumed to expand in all direction equally and any bipolar jets or strong clumping is avoided.
- **Radioactive heating:** For supernovae, radioactive decays of $^{60}\text{Ni} \rightarrow ^{56}\text{Co} \rightarrow ^{56}\text{Fe}$ ejects heat at exponential rate while kilonovae modeling uses a heating function derived from nucleosynthetic post-processing of numerical relativity simulations.

The energy evolution equation in this model is given by,

$$\boxed{\frac{dE}{dt} + p \frac{dV}{dt} = \dot{Q}_{decay} - L} \quad (1.1)$$

where,

- E is total internal radiation energy, $E = aT^4V$.
- P and V are pressure and specific volume respectively, $P = \frac{1}{3}aT^4$.
- $L(t)$ is the luminosity i.e. rate at which energy is escaping at outer boundary.
- \dot{Q}_{decay} is volumetric radioactive heating given by following equation,

$$\boxed{\dot{Q}_{decay}(t) = M_{Ni}[\epsilon_{Ni}e^{-t/\tau_{Ni}} + \epsilon_{Co}(e^{-t/\tau_{Co}} - e^{-t/\tau_{Ni}})]} \quad (1.2)$$

where,

- M_{Ni} is mass of ^{56}Ni synthesized,
- ϵ_{Ni} and ϵ_{Co} are the energy release rate per unit mass for each decay.
- τ_{Ni} and τ_{Co} are mean lifetime

Luminosity (bolometric) is calculated using the following equation (Derivation for this equation is given in the subsequent section),

$$L(t) = 2 \int_0^t \dot{Q}_{decay}(t') \frac{t - t'}{t_0^2} \exp \left[-\frac{(t - t')^2}{2t_0^2} \right] dt' \quad (1.3)$$

And then flux is calculated using the following equation,

$$F = -\frac{c}{3\kappa\rho} \frac{\partial(aT^4)}{\partial r} \quad (1.4)$$

where,

- F is flux in $\text{erg}/\text{s}/\text{cm}^2$
- κ is the opacity
- ρ is the density of medium
- aT^4 is the radiation energy density

1.1.3.1 Key Findings from Arnett's type II supernovae LC model:

- **Plateau Phase:** The shock wave deposits internal energy. The long-duration plateau arises because radiative diffusion competes with expansion cooling in the hydrogen envelope.
- **Diffusion Timescale:** $t_{\text{diff}} \propto \frac{\kappa M}{R(0)c}$ sets the approximate timescale for how quickly photons can escape, where $R(0)$ is the initial progenitor's radius.
- **Late Nebular Phase:** Once a large fraction of the mass is optically thin, these simple diffusion solutions break down and one must include nebular conditions.

1.1.3.2 Key findings from Arnett's type Ia supernovae LC model

The 1982 paper generalized Arnett's earlier method (for Type II) by explicitly including ^{56}Ni decay, ^{56}Co decay, and the growing transparency to gamma rays at late times.

- **Maximum-Light Condition:** A famous result:

$$\text{At the peak of the light curve, } L_{\max} \approx \dot{Q}_{\text{radioactive}}(t_{\max}).$$

Physically, when the light curve reaches maximum, the rate of photon diffusion out roughly balances the instantaneous heating from decays.

- **General Light-Curve Solutions** Arnett provided integral or tabulated forms for the time-dependent luminosity $L(t)$, typically written in dimensionless units. These incorporate exponentials for the nickel/cobalt decay and the time-dependent diffusion factor. The model can be used (given M_{Ni} , M , κ , v_{sc}) to produce approximate bolometric light curves and, with further assumptions, blackbody-like color evolution.
- **Large vs. Small Initial Radius** He also showed how a large initial progenitor radius $R(0)$ changes the *rise* to maximum, though for a compact white dwarf progenitor, the effect is minor and the radioactive power dominates.

1.1.4 Modification to Arnett's model for Kilonovae inclusion:

Several people, after Arnett, have modified his model to accommodate kilonovae produced by the mergers of BNS and NSBH. Matt Nicholl [26], along with his peers has developed an analytical model to fit the GW170817 (BNS merger) event. They achieved a Bayes factor of more than 10^{10} . Just by the inclusion of an additional luminosity source in addition to the previous lanthanide-poor dynamical ejecta.

Description of the Model:

The model separates the kilonova ejecta into different components, each associated with a physical mechanism and characterised by its mass, velocity, and opacity. In broad outline, the model includes:

- **Dynamical ejecta** produced during the merger via tidal stripping (primarily red, lanthanide-rich) and shock-heating (blue, lanthanide-poor) mass.
- **Post-merger ejecta** from viscous disk winds (“purple” component) whose mass depends on the lifetime of the remnant.
- Additional contributions from **magnetically-driven surface winds** or **shock cooling of a GRB cocoon** that may enhance the early blue luminosity.

The mass of the dynamical ejecta is derived using a fit to numerical relativity simulations [8]. The general form is given by:

$$\frac{M_{\text{dyn}}}{10^{-3}M_{\odot}} = \left[a \left(\frac{M_2}{M_1} \right)^{1/3} \left(\frac{1 - 2C_1}{C_1} \right) + b \left(\frac{M_2}{M_1} \right)^n + c \left(1 - \frac{M_1}{M_1^*} \right) \right] \frac{M_1^*}{1} + (1 \leftrightarrow 2) + d, \quad (1.5)$$

where

- M_1 and M_2 are the gravitational masses of the two Neutron Stars (by convention $M_1 \geq M_2$, so the mass ratio is defined as $q = M_2/M_1 \leq 1$),
- M_i^* are the corresponding baryonic masses, computed as $M_i^* = M_i + 0.08M_i^2$, and
- C_i is the compactness defined by

$$C_i = \frac{GM_i}{R_i c^2}. \quad (1.6)$$

Here $(1 \leftrightarrow 2)$ represents the exchange of subscript indices. The free parameters a , b , c , d , and n are determined from fits to simulation data. The key assumption here is that the dynamical ejecta mass is primarily controlled by the binary's mass ratio and the individual NS compactnesses (which depend on the NS radius and the EoS). Also, the dynamical ejecta is divided into **tidal ejecta** (red) and **shock-heated ejecta** (blue) based on the electron fraction Y_e .

The mass of the disk surrounding the remnant is parameterised using the following analytic expression from

Let's start from equation (1.1), let $E_{\text{int}}(t)$ be the internal energy of the ejecta at time t . The energy is injected at a rate $\dot{E}(t)$ (from radioactive decay \dot{Q}_{decay}) and lost via radiative diffusion. Furthermore, the work resulting from the first explosion, $p \frac{dv}{dt}$, contributes substantially less to the light curve over extended periods, making its contribution negligible. A simplified energy balance can be written as

$$\frac{dE_{\text{int}}(t)}{dt} = \dot{E}(t) - \frac{E_{\text{int}}(t)}{t_d}, \quad (1.7)$$

where t_d is the diffusion timescale given by

$$t_d = \left(\frac{2 \kappa M_{\text{ej}}}{\beta c v_{\text{ej}}} \right)^{1/2}. \quad (1.8)$$

where,

- κ is the ejecta opacity (often taken as a constant),
- M_{ej} is the ejecta mass,
- v_{ej} is the ejecta velocity,
- β is a geometric factor (usually of order unity), and
- c is the speed of light.

We solve the differential equation,

$$\frac{dE_{\text{int}}(t)}{dt} + \frac{E_{\text{int}}(t)}{t_d} = \dot{E}(t) \quad (1.9)$$

after multiplying by the integrating factor

$$\mu(t) = \exp \left(\int \frac{dt}{t_d} \right) = e^{t/t_d}$$

Thus,

$$\frac{d}{dt} [e^{t/t_d} E_{\text{int}}(t)] = e^{t/t_d} \dot{E}(t). \quad (1.10)$$

Integrating both sides from 0 to t , we have

$$e^{t/t_d} E_{\text{int}}(t) = \int_0^t e^{t'/t_d} \dot{E}(t') dt', \quad (1.11)$$

or equivalently,

$$E_{\text{int}}(t) = e^{-t/t_d} \int_0^t e^{t'/t_d} \dot{E}(t') dt'. \quad (1.12)$$

Since the emergent luminosity $L(t)$ is approximately given by the rate at which energy is released from the ejecta,

$$L(t) \approx \frac{E_{\text{int}}(t)}{t_d}, \quad (1.13)$$

we substitute the expression for $E_{\text{int}}(t)$ to obtain

$$L(t) \approx \frac{e^{-t/t_d}}{t_d} \int_0^t e^{t'/t_d} \dot{E}(t') dt'. \quad (1.14)$$

Defining a dimensionless time variable $\tau = t/t_d$ and $\tau' = t'/t_d$, the expression becomes

$$L(t) \approx \frac{e^{-\tau}}{t_d} \int_0^\tau e^{\tau'} \dot{E}(t_d \tau') t_d d\tau'. \quad (1.15)$$

Cancelling t_d , we have

$$L(t) \approx e^{-\tau} \int_0^\tau e^{\tau'} \dot{E}(t_d \tau') d\tau'. \quad (1.16)$$

A more refined treatment (see, e.g., Arnett 1982) shows that a better approximation is obtained when the integrand is weighted by τ' ; this leads to the solution

$$L(t) = 2 e^{-\tau^2} \int_0^\tau \tau' e^{\tau'^2} \dot{E}(t_d \tau') d\tau', \quad (1.17)$$

or, reverting back to t ,

$$L(t) = 2 e^{-\left(\frac{t}{t_d}\right)^2} \int_0^t \left(\frac{t'}{t_d}\right) e^{\left(\frac{t'}{t_d}\right)^2} \dot{E}(t') \frac{dt'}{t_d}. \quad (1.18)$$

1.1.5 Kilonovae from BNS vs. NSBH Mergers

While both BNS and neutron star-black hole (NSBH) mergers can produce kilonovae, the properties of these events differ due to the mass ejection mechanisms and the composition of the ejecta.

Ejecta Mass and Opacity

BNS Mergers: In binary neutron star mergers, both stars contribute to the ejecta. The total mass of this expelled matter usually falls between $0.0001M_\odot$ to $0.05M_\odot$. This ejecta consists of two main components: dynamical ejecta, caused by tidal forces during the merger, and disk winds, which result from post-merger accretion. [7]. The heavy r -process elements, particularly lanthanides, in the ejecta, increase the opacity, resulting in a redder kilonova signature that peaks in the infrared [14, 16].

NSBH Mergers: In neutron star-black hole (NSBH) mergers, the neutron star may be torn apart by the black hole's tidal forces, releasing ejecta. This only occurs if the disruption occurs outside the black hole's innermost stable circular orbit (ISCO). The amount of ejecta depends on the mass ratio, black hole spin, and the neutron star's equation of state (EoS). In this case, more mass is ejected if the neutron star has low mass and large deformability (i.e., it is easier for tidal forces to stretch and disrupt it). The black hole can tidally disrupt the neutron star, resulting in significant ejection of mass and thus producing a brighter kilonova. This situation results in optimal conditions for mass ejection, leading to a more luminous kilonova, the composition tends to be lighter in r -process elements, leading to a bluer, more optical-dominant kilonova [4, 12].

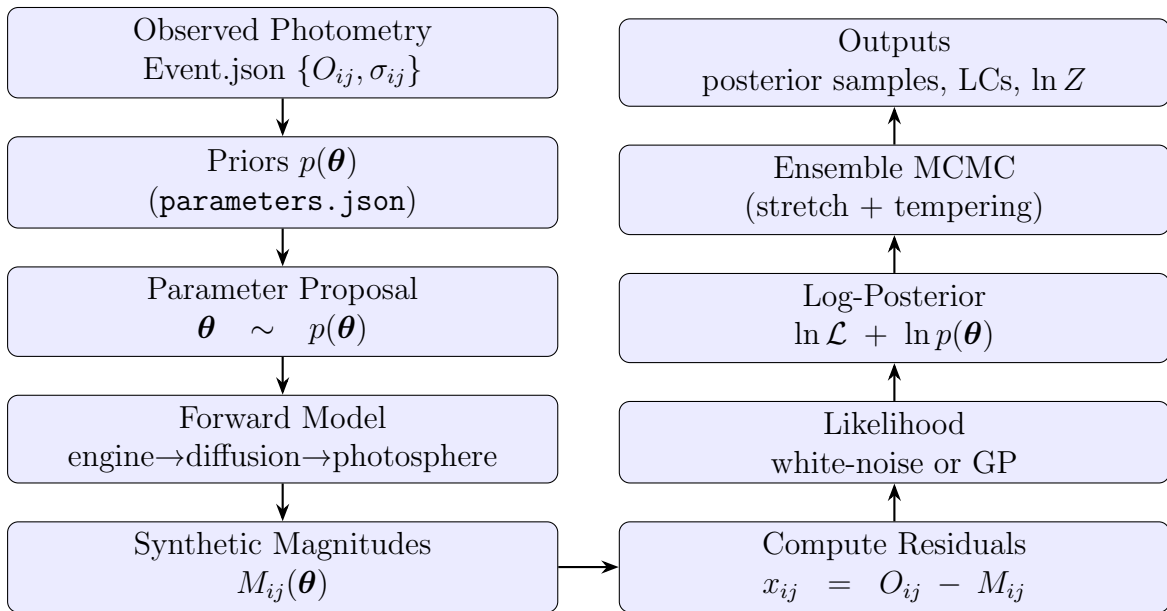
Electromagnetic Counterparts

The differences in the ejecta composition and opacity between BNS and NSBH mergers result in distinct electromagnetic signatures:

BNS Kilonovae: The high opacity from heavy r -process elements causes BNS kilonovae to appear dimmer and redder, peaking in the infrared wavelengths. The light curves are typically slower and less luminous due to the larger ejecta mass and higher opacity [4].
NSBH Kilonovae: In contrast, NSBH kilonovae tend to be brighter and peak faster, and the lighter elements lead to lower opacity. These kilonovae often peak in the optical wavelengths, producing a bluer transient than BNS mergers [31].

1.2 Introduction to Bayesian Inference in MOSFiT pipeline

The MODULAR OPEN-SOURCE FITTER FOR TRANSIENTS (MOSFiT; Guillochon *et al.* 2018) is designed to translate heterogeneous photometric data into physically interpretable model parameters in a fully Bayesian framework. The purpose of this memorandum is to explain, in prose rather than bullet points, how MOSFiT constructs the likelihood, combines it with user-defined priors, and ultimately delivers posterior samples, model evidence, and diagnostic statistics.



1.2.1 The Bayesian Framework

Let θ denote the vector of model parameters (ejecta mass, expansion velocity, opacity, explosion epoch, *etc.*), and let $\mathcal{O} = \{O_{ij}, \sigma_{ij}\}$ be the set of observed magnitudes (or fluxes) O_{ij} with quoted 1σ uncertainties σ_{ij} , recorded at times t_i and through filters j . Bayes' theorem states

$$p(\theta | \mathcal{O}) = \frac{p(\mathcal{O} | \theta) p(\theta)}{p(\mathcal{O})}, \quad (1.19)$$

where the *likelihood* $p(\mathcal{O} | \boldsymbol{\theta})$ quantifies how well a particular parameter set reproduces the data, the *prior* $p(\boldsymbol{\theta})$ encodes external astrophysical knowledge, and the denominator the *evidence* is a normalisation constant that is irrelevant for pure parameter estimation but essential for model comparison.

1.2.2 From Parameters to Synthetic Photometry

For every trial parameter vector the following deterministic pipeline is executed:

- (i) A call-tree, specified in the model’s JSON file, transforms the free parameters into physically meaningful time series: luminosity $L(t)$, photospheric radius $R(t)$, and temperature $T_{\text{phot}}(t)$.
- (ii) MOSFiT adopts a spectral-energy distribution (typically a black-body or a parametrically modified black-body), evaluates it at the epochs t_i , and convolution-integrates it through each instrumental transmission curve $S_j(\lambda)$. The outcome is a synthetic magnitude $M_{ij}(\boldsymbol{\theta})$ which can be compared directly to O_{ij} .

The residuals $x_{ij} = O_{ij} - M_{ij}(\boldsymbol{\theta})$ are the fundamental inputs to the likelihood.

1.2.3 Choice of Likelihood

MOSFiT offers two error models.

White-Noise (Independent-Error) Likelihood

If correlations between data points are negligible, the residuals may be treated as independent Gaussian variates. An additional variance parameter σ^2 captures unmodelled scatter. The log-likelihood is

$$\ln p(\mathcal{O} | \boldsymbol{\theta}) = -\frac{1}{2} \sum_{i,j} \left[\frac{x_{ij}^2}{\sigma_{ij}^2 + \sigma^2} + \ln(2\pi(\sigma_{ij}^2 + \sigma^2)) \right]. \quad (1.20)$$

Although simple, expression (1.20) is sufficient when the data set is sparse or when instrumental systematics dominate.

Gaussian-Process (Correlated-Error) Likelihood

Well-sampled light curves frequently exhibit correlations in time and colour that cannot be represented by a single variance term. In such circumstances MOSFiT defaults to a Gaussian process (GP) with a squared-exponential kernel

$$K_{ab} = \sigma^2 \exp \left[-\frac{(t_a - t_b)^2}{2\ell_t^2} - \frac{(\bar{\lambda}_a - \bar{\lambda}_b)^2}{2\ell_\lambda^2} \right] + \sigma_a^2 \delta_{ab}, \quad (1.21)$$

where ℓ_t and ℓ_λ are correlation lengths in time and effective wavelength, and σ^2 again measures additional scatter. With \mathbf{x} the vectorised residuals, the corresponding log-likelihood reads

$$\ln p(\mathcal{O} | \boldsymbol{\theta}) = -\frac{1}{2} \mathbf{x}^\top K^{-1} \mathbf{x} - \frac{1}{2} \ln |K| - \frac{N}{2} \ln(2\pi). \quad (1.22)$$

This treatment allows the model to borrow strength from neighbouring points and yields realistic uncertainty envelopes, particularly in filter bands that are sparsely sampled.

1.2.4 Specification of Priors

Priors are declared in the `parameters.json` file. Common choices are uniform or log-uniform bounds on ejecta mass (10^{-3} – $1 M_\odot$), opacity (0.1 – $100 \text{ cm}^2 \text{ g}^{-1}$), and explosion epoch (a uniform window bracketing the first observation). If a proposal violates any prior bound, MOSFiT assigns the value $-\infty$ to $\ln p(\boldsymbol{\theta})$, causing the sampler to reject it immediately.

1.2.5 Posterior Evaluation

For each trial the *unnormalised* log-posterior is formed as the sum

$$\ln p(\boldsymbol{\theta} | \mathcal{O}) = \ln p(\mathcal{O} | \boldsymbol{\theta}) + \ln p(\boldsymbol{\theta}),$$

using either equation (1.20) or (1.22) for the first term.

1.2.6 Sampling Strategy

MOSFiT relies on the parallel-tempered, affine-invariant ensemble sampler implemented in EMCEE. The procedure is:

1. *Pre-burn phase*: a short Gibbs-style randomisation helps the walker ensemble escape obvious local minima (detailed balance is intentionally suspended).
2. *Main burn-in*: the affine-invariant stretch move runs at multiple temperatures; detailed balance is restored.
3. Convergence is diagnosed with the Gelman–Rubin potential-scale-reduction factor, requiring $\hat{R} < 1.1$ for every parameter.
4. Once converged, the chain is thinned by the integrated autocorrelation time to yield effectively independent samples.

1.2.7 Evidence and Model Comparison

If requested, MOSFiT estimates the marginal likelihood (“evidence”) via thermodynamic integration over the parallel-tempering ladders. Models A and B are compared through the Bayes factor $\text{BF}_{AB} = Z_A/Z_B (= e^{\ln Z_A - \ln Z_B})$. In most practical applications a factor $\text{BF} \gtrsim 10$ is already regarded as strong support for the favoured model.

1.2.8 Outputs

The code writes a single JSON file containing:

- every posterior sample (parameter values and likelihood);
- summary statistics (median and $\pm 1\sigma$ credible limits);
- optional synthetic light curves evaluated from a user-selected subset of samples;
- convergence metrics, the WAIC score, if requested the evidence $\ln Z$.

These artefacts allow full reproducibility and facilitate immediate visual inspection of the model fit.

Through a transparent combination of explicitly declared priors, flexible likelihood functions, and a modern ensemble sampler, MOSFiT provides a statistically rigorous route from raw transient photometry to physically meaningful parameter constraints. The same machinery can be harnessed not only for model fitting but also, via the evidence, for formal Bayesian model selection.

1.3 Introduction to Bayesian Inference in Gravitational Wave Physics:

1.3.1 Introduction

Bayesian inference has emerged as an important tool in the gravitational wave (GW) astronomy frontier. Detecting gravitational waves, which are faint ripples in spacetime caused by violent cosmic events such as binary black hole mergers, requires sophisticated statistical tools to interpret weak signals buried in noise. This section introduces Bayesian inference and how it is useful in gravitational-wave physics, also outlines its benefits over traditional frequentist methods, and discusses its applications in parameter estimation and model selection.

1.3.2 The Role of Bayesian Inference in Gravitational-Wave Physics

Gravitational-wave astronomy presents unique challenges in data analysis due to the weak and transient nature of signals with GW strain of the order 10^{-21} [28] and the complex noise environment in which they are detected. Bayesian inference is well structured to face these challenges, allowing researchers to incorporate prior knowledge, and uncertainty, and update beliefs based on observed data. This contrasts with frequentist approaches, where parameters are fixed and estimation relies on repeated sampling or specific assumptions about experiment repetition [30, 13].

Within the Bayesian paradigm, the parameters characterising a gravitational wave source, such as the masses, spins, and sky coordinates of the binary, are seen as stochastic variables. The aim is to assess the posterior probability distribution of these parameters using the data observation and existing information. The uncertainty in the parameter values are fully described by this posterior distribution in a probabilistic manner.

Bayesian Inference vs Frequentist Methods

In frequentist statistics, the estimation of parameters involves the construction of confidence intervals based on hypothetical repetitions of an experiment. However, events like black hole mergers are rare in gravitational-wave astronomy. Bayesian inference does not rely on repetitions, but instead updates the probability distribution of the unknown parameters based on the observed data [13]. This is especially advantageous in gravitational wave detection, which deals with a single observation of a unique cosmic event.

1.3.3 Key Concepts of Bayesian Inference

Bayesian inference is based upon Bayes' Theorem, which relates the posterior probability distribution $p(\theta|d)$ of the model parameters θ to the likelihood $L(d|\theta)$, the prior probability $p(\theta)$, and the evidence $p(d)$:

$$p(\theta|d) = \frac{L(d|\theta)p(\theta)}{p(d)} \quad (1.23)$$

Here, d represents the observed data (in this case, the strain data from gravitational-wave detectors), and $p(d)$ is the evidence, serving as a normalisation factor. The likelihood $L(d|\theta)$ describes how likely the observed data is, given a particular set of parameters, while the prior $p(\theta)$ is a known parameter [30, 13] which we inject in the signal.

Likelihood Function

The likelihood function is a core component of Bayesian inference. It encapsulates the probability of observing the data d given the model parameters θ . In gravitational wave detection, the likelihood is often based on a Gaussian noise model with an additive signal from a binary merger event. For example, for a network of detectors, the likelihood function may be represented as:

$$L(d|\theta) = \exp\left(-\frac{1}{2} \sum_{i=1}^N \frac{(d_i - h(\theta)_i)^2}{\sigma_i^2}\right) \quad (1.24)$$

where d_i is the observed strain at time i , $h(\theta)_i$ is the predicted strain based on the model parameters θ , and σ_i is the noise variance [30, 25].

Priors

Priors $p(\theta)$ express our knowledge or assumptions about the parameter values before observing the data. In gravitational-wave astronomy, priors can be informed by previous detections, and astrophysical models, or be chosen to reflect ignorance (e.g., uniform or log-uniform distributions for unknown parameters)[13].

The prior choice can significantly affect the results, especially when the data is not strongly informative. In some cases, informative priors based on previous detections are used to narrow down the parameter space, whereas uninformative priors are used when little prior knowledge is available.

Posterior Distribution

The posterior distribution $p(\theta|d)$ combines the likelihood and prior, providing the updated belief about the parameter values after considering the data. This posterior is used to make inferences about the physical parameters of a gravitational wave event, such as the component masses, spins, and distances of merging objects [13].

1.3.4 Parameter Estimation and Model Selection

Finding the most likely values of source parameters (such as masses, spins, tidal deformability, spin orientation, and sky location) from the observed data is known as parameter estimation. It is one of the primary applications of Bayesian inference in gravitational

wave astronomy. Bayesian methods also allow hypothesis testing and model selection by comparing the evidence Z for different models [30, 25].

Parameter Estimation

Parameter estimation involves computing the posterior distribution over the parameter space. This can be computationally challenging, especially given the high dimensionality of the parameter space in binary black hole mergers, which can involve up to 15 parameters. Methods like Markov Chain Monte Carlo (MCMC) and nested sampling are used to efficiently explore this space

Model Selection and Bayesian Evidence

In Bayesian model selection, the evidence Z for a given model is computed by marginalising over all possible parameter values:

$$Z = \int L(d|\theta)p(\theta)d\theta \quad (1.25)$$

This evidence is used to compare different models by computing the Bayes factor defined as the ratio of evidence between two models:

$$BF_{ij} = \frac{Z_i}{Z_j} \quad (1.26)$$

A Bayes factor generally greater than one or more¹ indicates that model i is more strongly supported by the data than model j , and vice versa [30]. This is useful for testing competing astrophysical models, such as comparing general relativity predictions with alternative theories of gravity.

1.3.5 Computational Methods for Bayesian Inference

Given the complexity of gravitational-wave signals and the large number of parameters involved, direct evaluation of the posterior distribution via integration in higher-dimensional space is computationally infeasible. Instead, advanced stochastic sampling methods such as MCMC and nested sampling are employed.

Markov Chain Monte Carlo (MCMC)

MCMC is a popular method for sampling from the posterior distribution. In this approach, a set of "walkers" explore the parameter space, with their movement governed by a transition probability that ensures convergence to the target posterior distribution. MCMC is widely used in gravitational-wave astronomy due to its flexibility and efficiency in high-dimensional spaces [30, 25]. There are several MCMC samplers available for Bayesian inference, like emcee, pymc, zeus etc.

¹It's an individual choice for fixing the Bayes factor. Some individuals can set it as 10 some others can set it as 100.

Nested Sampling

Nested sampling is another technique used to compute both the posterior distribution and the evidence. It transforms the multi-dimensional integral over the likelihood into a one-dimensional one, making it particularly effective for model selection problems where the evidence plays a central role [30]. There are numerous nested samplers available for Bayesian inference, like Dynesty, Nestle, PyPolyChord, etc.

Chapter 2

Motivation

The need to distinguish between neutron star-black hole (NSBH) and binary neutron star (BNS) mergers is becoming increasingly critical as more gravitational wave events are detected, particularly those involving masses within the so-called "mass gap." As these systems often have similar gravitational wave signatures, it becomes challenging to confidently predict the type of merger (NSBH or BNS) based on gravitational wave data alone. Additionally, these mergers produce comparable electromagnetic signatures, though in different proportions, further complicating the classification.

One of the main motivations behind this study is to improve our ability to distinguish between these two types of mergers, even in cases where the individual components' masses fall within the mass gap. Kilonovae, which are associated with the mergers of compact objects like neutron stars, provide valuable multi-messenger information that can be leveraged to differentiate between NSBH and BNS mergers.

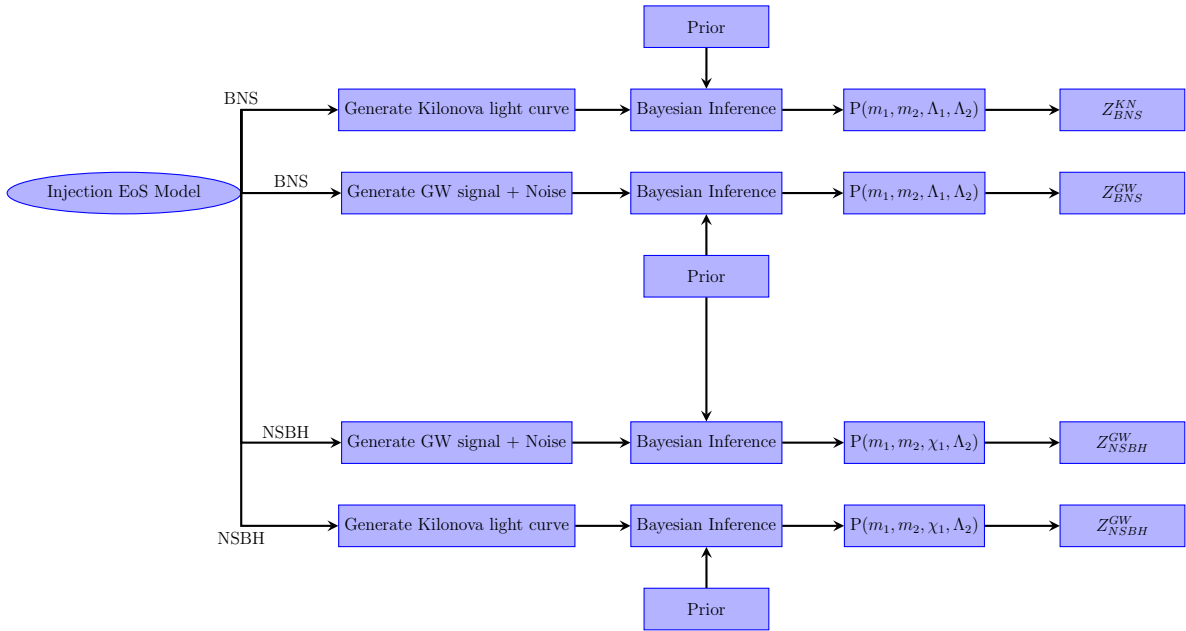
Key differences in the properties of the ejecta, such as the ejecta mass and the time to peak of the kilonova light curve, offer critical clues. BNS mergers tend to have a lower ejecta mass and a slower light curve, while NSBH mergers tend to result in a higher ejecta mass and a faster peak in the kilonova light curve. These differences can be used to classify the mergers and better understand the astrophysical processes driving them. Ultimately, distinguishing between these merger types is important not only for heavy element nucleosynthesis but also for identifying low-mass black holes and measuring black hole spins in NSBH systems, all of which have significant implications for our understanding of compact object mergers and the cosmic origins of heavy elements.

Chapter 3

Methodology

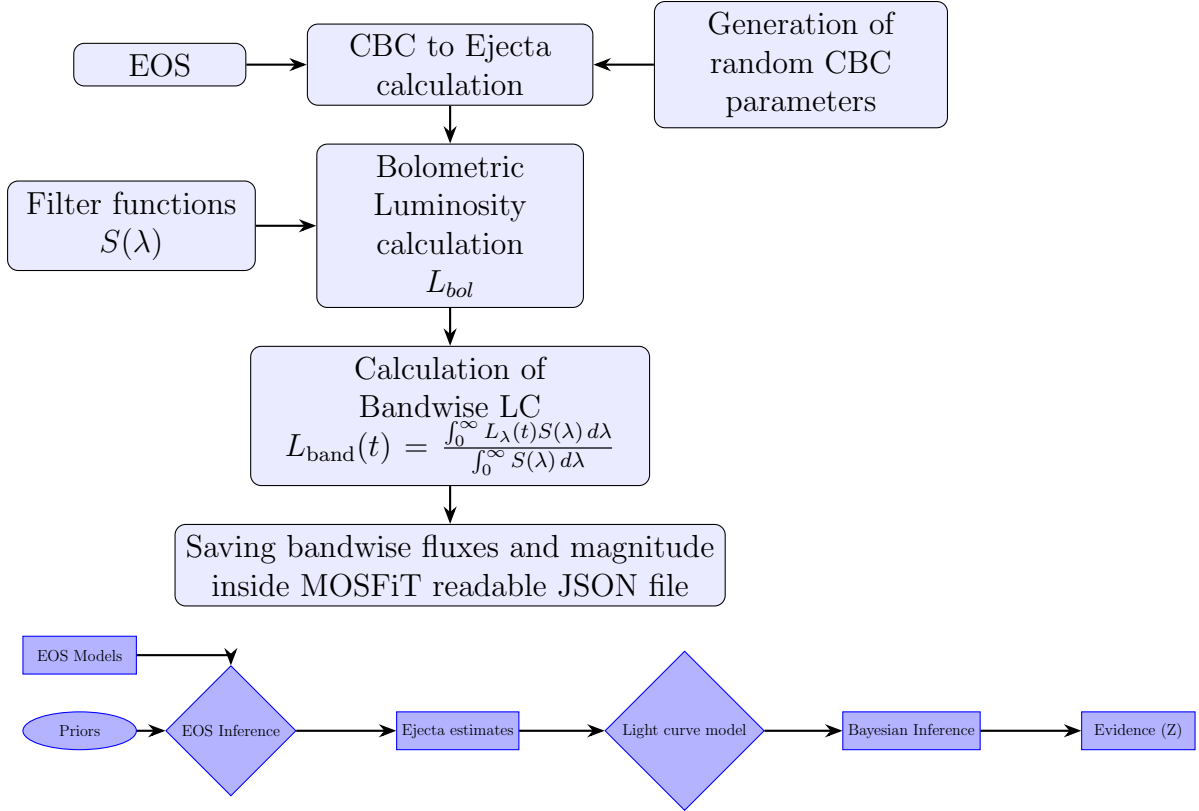
This project uses Bayesian inference to distinguish kilonovae resulting from neutron star–black hole (NSBH) and binary neutron star (BNS) mergers. Bilby Python library, an open-source module built on the LIGO Algorithm Library Suite (LAL) will be employed for gravitational wave (GW) inference, while MOSFiT will be used for kilonova analysis. This approach prioritises Bayesian methods over population modelling and frequentist inference.

3.1 Flowchart:



The flowchart outlines the analytical workflow adopted for this project. We will perform Kilonova inference using MOSFiT to generate light curves and perform parameter estimation. Also, we will be using Bilby for gravitational wave inference. We will then compare the Bayes Factor given by both pipelines to evaluate the preference of the model. Additionally, we will also plot a contour map of both pipelines for a given model to check which pipeline is more robust[3, 23].

3.1.1 Kilonova Inference

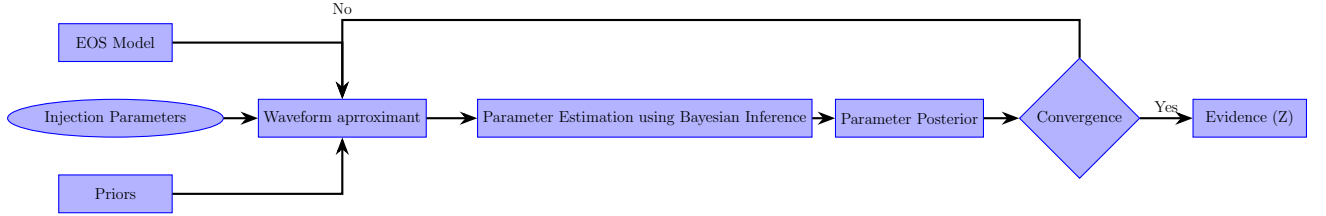


To perform kilonova inference, we will use **MOSFiT** (Modular Open Source Fitter for Transients) [15], which contains a large library of events such as GW170817 and supernovae. The main pipeline in MOSFiT conducts Bayesian inference on parameters such as L_{Bol} (bolometric luminosity), κ (opacity), m_{ejecta} (ejecta mass), and d_L (luminosity distance) etc. to create light curve. We will be using a modified MOSFiT model which will allow it to use the parameters which are consistent with those used in GW inference via the Bilby library such as $(m_1, m_2, \chi_1, \Lambda_2)$ for Neutron Star-Black Hole (NSBH) mergers and $(m_1, m_2, \Lambda_1, \Lambda_2)$ for Binary Neutron Star (BNS) mergers. By incorporating different Kilonova models, we will determine which model is most favoured. To quantitatively assess model preference, we define the Bayes factor as:

$$BF = \frac{Z_{NSBH}}{Z_{BNS}} \quad (3.1)$$

where Z_{NSBH} and Z_{BNS} denote the Bayesian evidence for NSBH and BNS models, respectively. We will use fiducial values of $BF > 5, 10, 100$, we conclude that the selected model favours NSBH; otherwise, BNS is favoured. To identify which model and prior combination has the least error band, we will use a modified version of MOSFiT to create light curves for both the BNS and NSBH models. We will choose the best model and prior based on this study and put them into the Bilby pipeline. The following subsection discusses the process for obtaining the Bayes Factor from the Bilby pipeline.

3.1.2 GW Inference:



We will inject parameters and priors which we have obtained from the kilonova inference such as $(m_1, m_2, \chi_1, \Lambda_2)$ for Neutron Star-Black Hole (NSBH) mergers and $(m_1, m_2, \Lambda_1, \Lambda_2)$ for Binary Neutron Star (BNS) mergers into our pipeline. For each case, we will select an Equation of State (EOS) model for the neutron star, focusing on the APR4, SLy, and DD2 models. We will use **IMRPhenomTidalv2** as the waveform approximant for BNS systems and **IMRPhenomNSBH** for NSBH systems. After performing Bayesian inference on this data, we will verify whether the injected parameters are recovered. If we cannot recover them, we will identify which parameters are not converging and modify the waveform approximant accordingly. After recovering all injected parameters, we will calculate the Bayes factor in eq 3.1.

3.2 Calculating BNS Lightcurve:

We use...

3.2.1 General Structure

For the total ejecta mass, M_{ej} , is composed of two parts [19]:

$$M_{\text{ej}} = M_{\text{ej,dyn}} + (f_{\text{wind}} + f_{\text{visc}}) M_{\text{ej,disk}}, \quad (3.2)$$

where f_{wind} and f_{visc} (often taken as ~ 0.15 each) represent the fractions of the disk mass converted into ejecta.

3.2.2 Dynamical Ejecta

For prescriptions such as “Radice2018a” or “Nedora2020Eq91217”, the dynamical ejecta mass is computed via intermediate quantities:

$$a = \alpha \left(\frac{M_b}{M_a} \right)^{1/3} \frac{1 - 2C_a}{C_a} + \beta \left(\frac{M_b}{M_a} \right)^n + \gamma \left(1 - \frac{M_a}{M_{a,\text{Baryonic}}} \right), \quad (3.3)$$

$$b = \alpha \left(\frac{M_a}{M_b} \right)^{1/3} \frac{1 - 2C_b}{C_b} + \beta \left(\frac{M_a}{M_b} \right)^n + \gamma \left(1 - \frac{M_b}{M_{b,\text{Baryonic}}} \right), \quad (3.4)$$

and then

$$M_{\text{ej,dyn}} = [a + b + \delta] M_{\odot} \times 10^{-3}. \quad (3.5)$$

Here:

- M_a and M_b are the gravitational masses of the two neutron stars (in M_\odot).
- C_a and C_b are their compactness parameters.
- $M_{a,\text{Baryonic}}$ and $M_{b,\text{Baryonic}}$ denote the baryonic masses.
- $\alpha, \beta, \gamma, \delta, n$ are fitting parameters that vary between prescriptions.

3.2.3 Disk Wind Ejecta

A typical prescription for the disk wind component is written as:

$$M_{\text{ej,disk}} = M_\odot \times \max \left(10^{-3}, \alpha + \beta \tanh \left(\frac{\tilde{\Lambda} - \gamma}{\delta} \right) \right), \quad (3.6)$$

with

$$\tilde{\Lambda} = \frac{(11M_b + M)\lambda_a/M_a + (11M_a + M)\lambda_b/M_b}{26}, \quad (3.7)$$

and where $M = M_a + M_b$. In some fits, the total ejecta mass takes the alternative form[27]:

$$M_{\text{ej}} = M_\odot \max \left(5 \times 10^{-4}, \alpha + \beta \tanh \left(\frac{\tilde{\Lambda} - \gamma}{\delta} \right) \right). \quad (3.8)$$

3.2.4 Ejecta Velocity Calculation

The ejecta velocity v_{ej} is given by:

$$a = \alpha \frac{M_a}{M_b} (1 + \gamma C_a), \quad (3.9)$$

$$b = \alpha \frac{M_b}{M_a} (1 + \gamma C_b), \quad (3.10)$$

and then

$$v_{\text{ej}} = [a + b + \beta] c, \quad (3.11)$$

where c is the speed of light and the coefficients depend on the chosen prescription.

3.2.5 Light Curve Heating Rate

Radioactive Heating Rate [21]

The heating rate per unit time is given by:

$$L_{\text{in}}(t) = \epsilon_0 2 M_{\text{rp}} \left[0.5 - \frac{1}{\pi} \arctan \left(\frac{t - t_0}{s} \right) \right]^{1.3}, \quad (3.12)$$

where:

- M_{rp} is the mass of radioactive ejecta.
- t is the time since the merger.

- t_0 and s are fitting parameters.
- ϵ_0 is a normalization constant (e.g., 2×10^{18} in cgs units).

Variants of this function (e.g., $L_{\text{in},\text{Ricigliano2021}}$) modify the parameters or behavior at early/late times.

Thermalization Efficiency

The thermalization efficiency is given by [5]:

$$\epsilon_{\text{th}}(t) = 0.36 \left[e^{-at} + \frac{\ln(1 + 2bt^d)}{2bt^d} \right], \quad (3.13)$$

where a , b , and d are determined via interpolation based on the ejecta velocity (in units of c) and M_{rp} .

Net Heating Rate

The net heating rate is the product of the heating rate and the thermalization efficiency:

$$Q_{\text{net}}(t) = L_{\text{in}}(t) \epsilon_{\text{th}}(t). \quad (3.14)$$

3.2.6 Diffusion and Bolometric Luminosity

Diffusion Timescale

The effective diffusion timescale is estimated as:

$$t_d = \sqrt{\frac{2\kappa M_{\text{rp}}}{\beta v c}}, \quad (3.15)$$

where

- κ is the opacity.
- v is the ejecta velocity.
- β is a constant (set to 13.8 in the code).

Bolometric Luminosity

The bolometric luminosity is modelled as:

$$L_{\text{bol}}(t) = \exp\left(-\frac{t^2}{t_d^2}\right) \int_0^t L_{\text{in}}(t') \epsilon_{\text{th}}(t') \exp\left(\frac{t'^2}{t_d^2}\right) \frac{t'}{t_d} dt'. \quad (3.16)$$

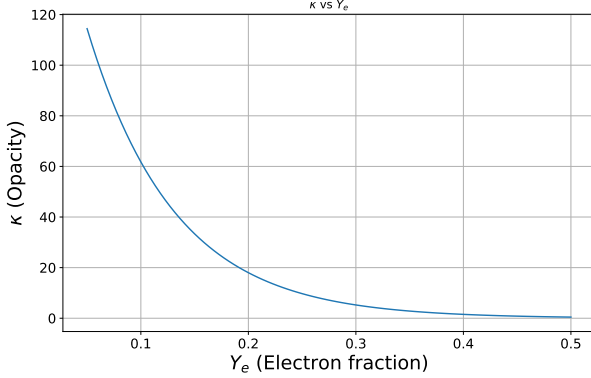


Figure 3.1: Plot between κ and Y_e showcasing decrease of opacity with increase in electron fraction

Opacity [9]

The opacity κ is given by,

$$\kappa = 211.98 \times e^{-12.33 \times Y_e} \quad (3.17)$$

The plot is given by,

This counterintuitive trend can be explained by following reasons,

- Heavier r-process elements (lanthanides, actinides) form when the material is very neutron-rich. These elements have extremely complex atomic structures with many bound-bound transitions, which significantly increase the total opacity.
- In a fully ionized plasma, the electron scattering opacity is proportional to the number of free electrons per gram. But, in r-process ejecta the contribution from opacities dominated by heavy elements overwhelms the simple electron scattering term.

3.2.7 Photospheric Emission

Temperature

The photospheric temperature is estimated via a blackbody relation:

$$T_{\text{phot}} = \left(\frac{L}{4\pi\sigma_B (v t)^2} \right)^{1/4}, \quad (3.18)$$

with a lower cutoff temperature, T_c (e.g., 3000 K):

$$T_{\text{phot}} = \max \left[\left(\frac{L}{4\pi\sigma_B (v t)^2} \right)^{1/4}, T_c \right]. \quad (3.19)$$

Photospheric Radius

The photospheric radius is given by:

- $R_{\text{phot}} = v t$ when $T_{\text{phot}} > T_c$,
- and if $T_{\text{phot}} \leq T_c$, then

$$R_{\text{phot}} = \left(\frac{L}{4\pi\sigma_B T_c^4} \right)^{1/2}.$$

3.2.8 Blackbody Emission and AB Magnitude

Planck Function

The spectral radiance per unit frequency is given by:

$$B_\nu(T) = \frac{2 h \nu^3}{c^2} \frac{1}{\exp(\frac{h\nu}{kT}) - 1}, \quad (3.20)$$

and per unit wavelength by:

$$B_\lambda(T) = \frac{2 h c^2}{\lambda^5} \frac{1}{\exp(\frac{hc}{\lambda kT}) - 1}. \quad (3.21)$$

AB Magnitude

The AB magnitude corresponding to a flux density f_ν (in $\text{erg s}^{-1} \text{cm}^{-2} \text{Hz}^{-1}$) is:

$$m_{AB} = -2.5 \log_{10}(f_\nu) - 48.6. \quad (3.22)$$

3.2.9 Gravitational Wave Related Quantities

Chirp Mass

The chirp mass is defined as:

$$\mathcal{M}_c = \frac{(m_1 m_2)^{3/5}}{(m_1 + m_2)^{1/5}}. \quad (3.23)$$

Symmetric Mass Ratio

The symmetric mass ratio is:

$$\eta = \frac{q}{(1+q)^2}, \quad (3.24)$$

where $q = \frac{m_2}{m_1}$ and it is assumed that $m_1 \geq m_2$.

3.3 Calculating NSBH Lightcurve:

3.3.1 ISCO Radius

The innermost stable circular orbit (ISCO) radius for a black hole with mass M_{bh} and spin χ_{bh} is:

$$R_{\text{ISCO}} = M_{\text{bh}} \left[3 + Z_2 - \text{sign}(\chi_{\text{bh}}) \sqrt{(3 - Z_1)(3 + Z_1 + 2Z_2)} \right] \quad (3.25)$$

where:

$$Z_1 = 1 + (1 - \chi_{\text{bh}}^2)^{1/3} \left[(1 + \chi_{\text{bh}})^{1/3} + (1 - \chi_{\text{bh}})^{1/3} \right] \quad (3.26)$$

and

$$Z_2 = \sqrt{3\chi_{\text{bh}}^2 + Z_1^2} \quad (3.27)$$

3.3.2 Remnant Mass

The remnant mass M_{rem} for a neutron star-black hole merger is calculated using:

$$M_{\text{rem}} = M_{\text{ns}} \left[a (1 - 2C_{\text{ns}}) \eta^{-1/3} - b \cdot R_{\text{ISCO}} \cdot C_{\text{ns}} \eta + g \right]^d \quad (3.28)$$

where $\eta = \frac{q}{(1+q)^2}$ is the symmetric mass ratio, $q = \frac{M_{\text{bh}}}{M_{\text{ns}}}$, and C_{ns} is the compactness of the neutron star.

3.3.3 Dynamical Ejecta Mass

The dynamical ejecta mass M_{dyn} is given by:

$$M_{\text{dyn}} = M_{\text{ns}} \times \max \left[a_1 (q^{n_1}) \frac{1 - 2C_{\text{ns}}}{C_{\text{ns}}} - a_2 \cdot R_{\text{ISCO}} \cdot (q^{n_2}), 0 \right] \quad (3.29)$$

where a_1, a_2 are constants, n_1, n_2 are exponents, and C_{ns} is the compactness of the neutron star.

3.3.4 Unbound Disk Mass

The unbound disk mass is calculated by:

$$M_{\text{disk}} = M_{\text{rem}} - M_{\text{dyn}}, \quad (3.30)$$

and adjusted using:

$$w_{\text{frac}} = c_1 + \frac{c_2 - c_1}{1 + \exp(1.5(q - 3))}, \quad (3.31)$$

where $q = \frac{M_{\text{bh}}}{M_{\text{ns}}}$ is the mass ratio.

3.3.5 Ejecta Velocity

The ejecta velocity v_{ej} is modeled as a linear relation:

$$v_{\text{ej}} = 0.0149 q + 0.1493 \quad (3.32)$$

where $q = \frac{M_{\text{bh}}}{M_{\text{ns}}}$.

3.4 Calculating Bandwise Lightcurve:

A filter transmission function defines each photometric band (e.g., U, B, V) $S(\lambda)$ (or $S(\nu)$ in frequency space). The bandwise luminosity (or flux) is obtained by integrating the product of the blackbody spectrum and the filter response over wavelength (or frequency):

$$L_{\text{band}}(t) = \frac{\int_0^\infty L_\lambda(t) S(\lambda) d\lambda}{\int_0^\infty S(\lambda) d\lambda}. \quad (3.33)$$

Chapter 4

Progress and Results

4.1 NSBH results

Up until now, we have been able to generate some useful results in terms of GW inference on the current IIT Bombay Spacetime cluster. However, we were able to get some useful insights from the NSBH runs and BNS runs that we obtained by running through LIGO cluster. The BNS runs are producing some good results in the graphs below.

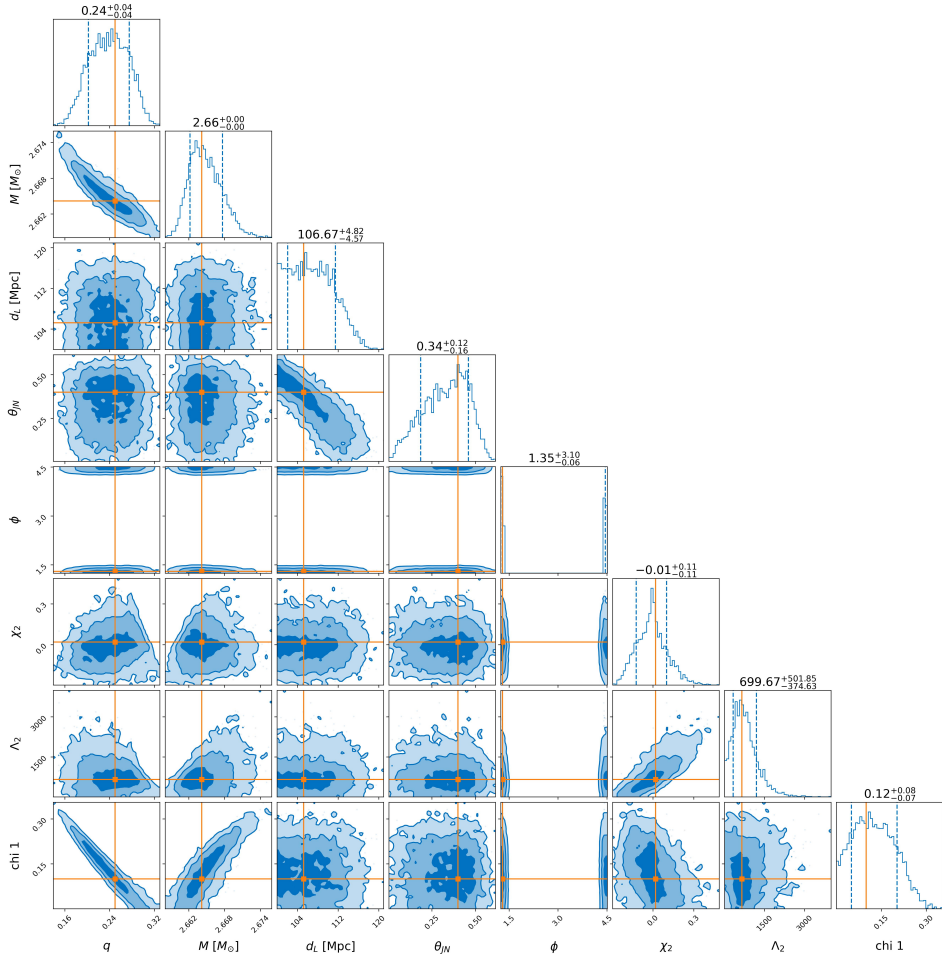


Figure 4.1: A Sample 8 parameter NSBH Corner plot generated using **IMRPhenomNSBH** waveform approximant with nested sampler **dynesty** was used with $q = 0.25$

The corner plot generated above was simply to check the compatibility of the waveform approximant **IMRPhenomNSBH**. The above-generated corner plots show that we have recovered almost all the injected parameters within the given values. In this run we have kept $\Lambda_1 = 0$, since the m_2 injected in this run is $> 5M_\odot$. Hence the waveform approximant is well suited for NSBH runs. Following are the values of injected parameters used for the above run. The tidal deformability Λ_2 of the neutron star of mass m_2 has been taken from [20] this literature.

Parameters	Injected values
m_1	$6.4M_\odot$
m_2	$1.6M_\odot$
Λ_2	650

Table 4.1: *Injected parameters and their values for sample NSBH run from figure 4.1*

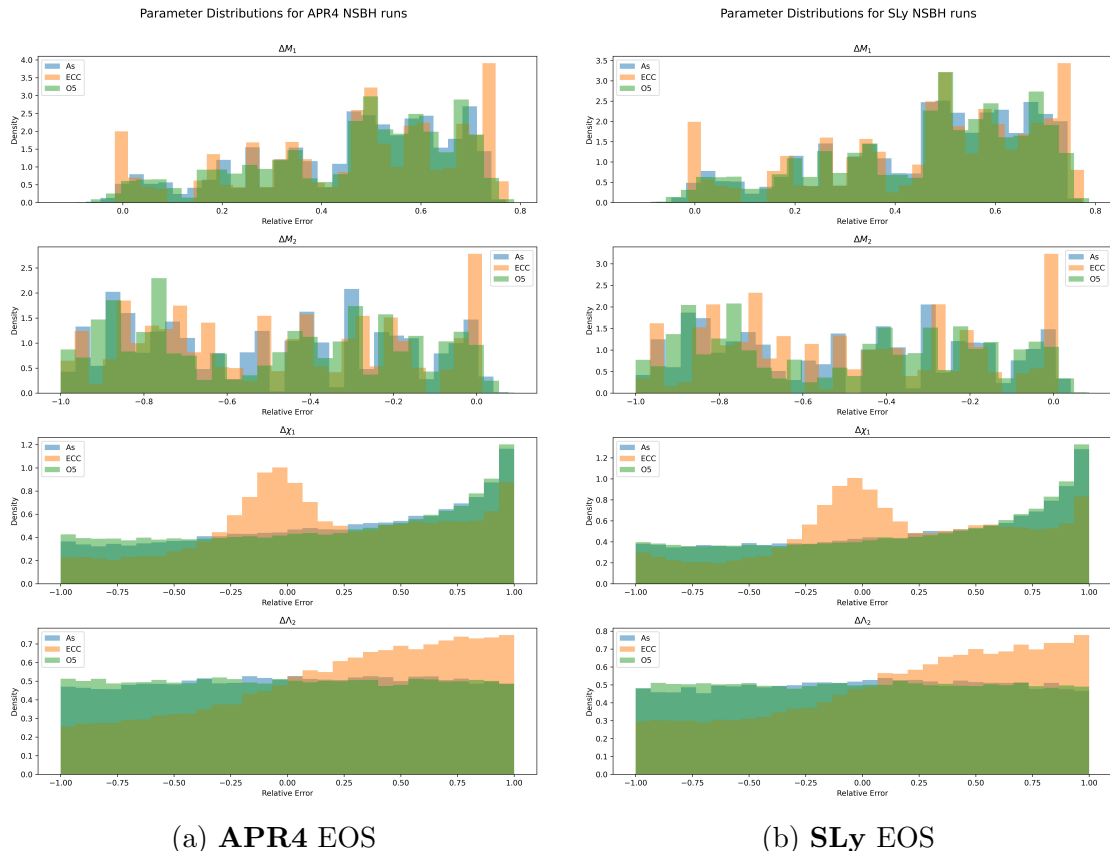


Figure 4.2: *Comparisons between relative errors in 4 parameters among 100 NSBH runs for 3 detectors using **IMRPhenomTidalv2** waveform approximant for **APR4** and **SLy EOS***

The above generated graphs depict the three detectors' accuracy over two equations of states for 4 parameters incorporating 100 runs for each detector for relative errors in the measurement of the parameters. In these runs we kept both the tidal deformabilities as free parameters i.e. we have not forced any low or high mass runs to be NSBH or BNS specific. We can infer from this graph that the waveform approximant that we used **IMRPhenomTidalv2** is not appropriate for performing inference on the NSBH system

as even for the most sensitive detector the values of errors are too large. This can be inferred from fig4.4 and fig4.5 Also for the high mass system, we should fix $\Lambda_1 = 0$ and use **IMRPhenomNSBH** approximant to get better results. All the above runs were made using **dynesty** sampler.

Following are the corner plots corresponding to the best runs depicting injected values of the mass of the heavier companion is in the mass gap. This suggests that we should run low mass systems using **IMRPhenomTidalv2** by keeping both the tidal deformability as free parameters.

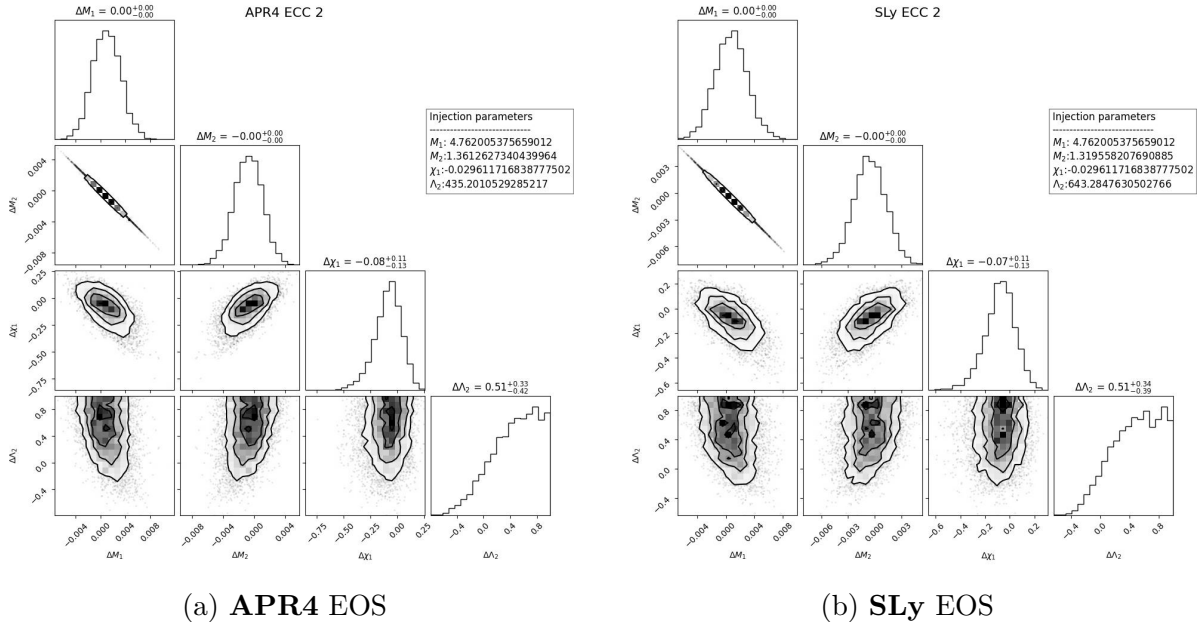


Figure 4.3: *Corner plots of best runs for NSBH for ECC detectors using IMRPhenomTidalv2 waveform approximant for APR4 and SLy EOS*

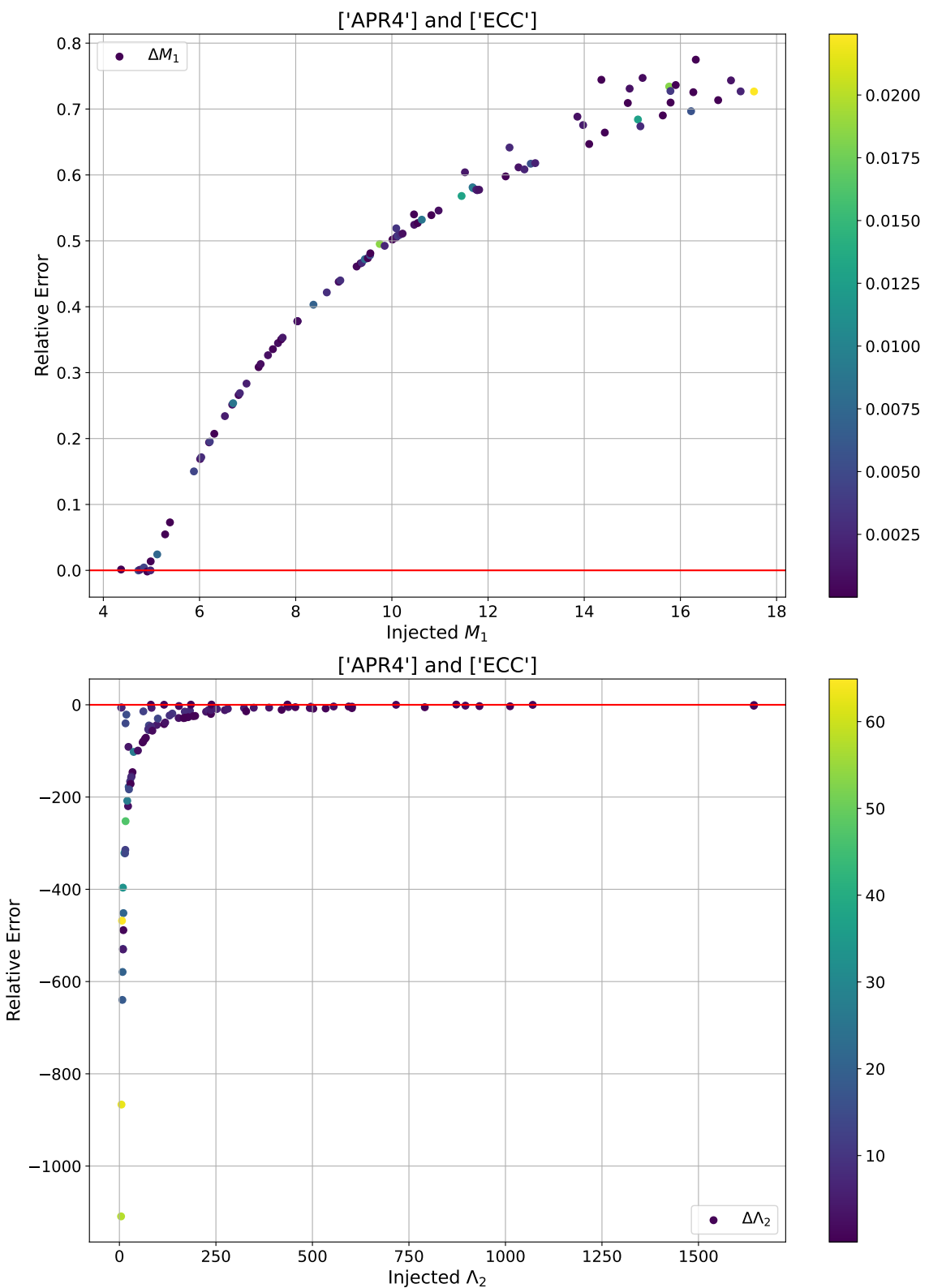


Figure 4.4: Subplots of relative errors versus injected parameters for ECC detector with **APR4** EoS

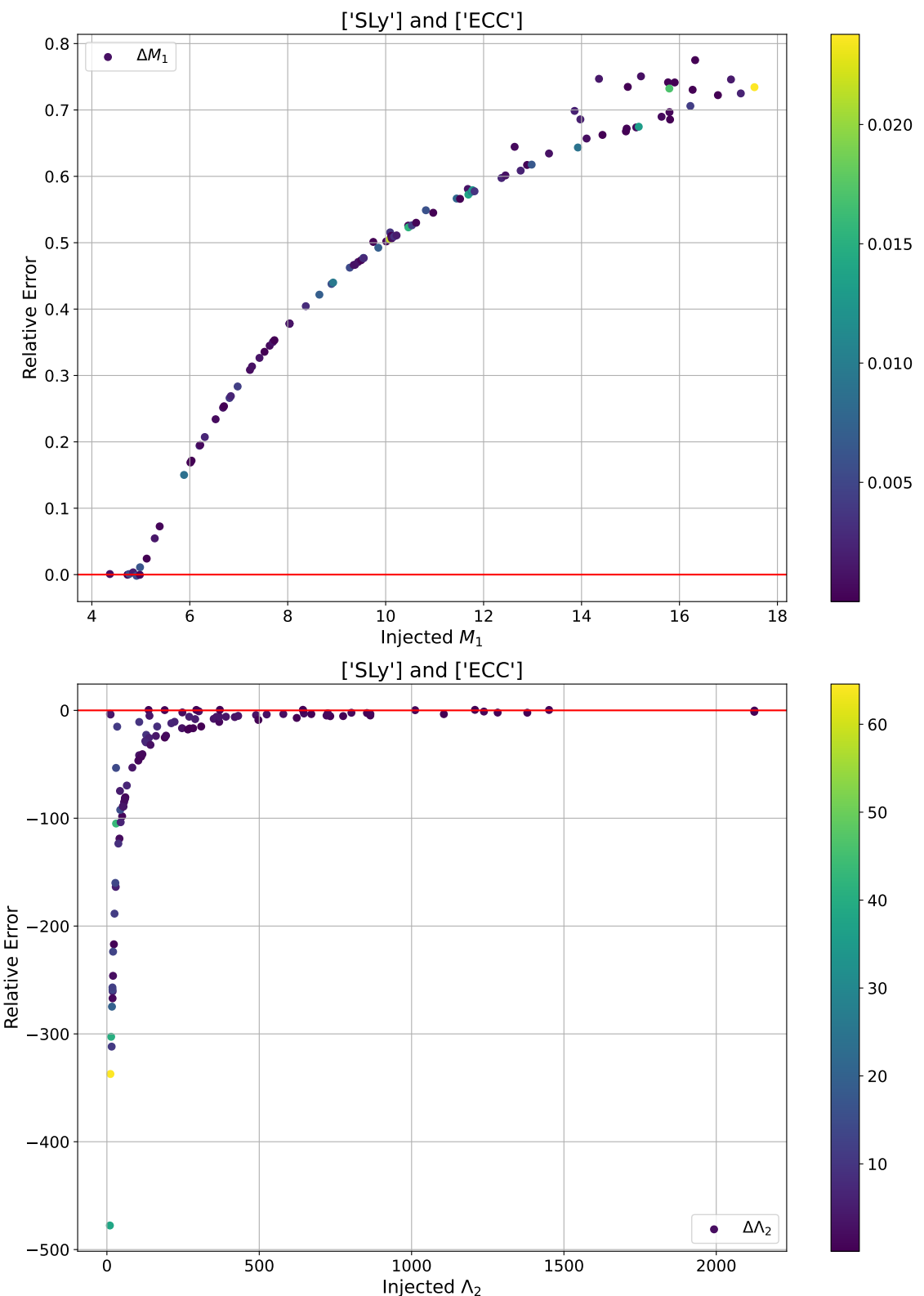


Figure 4.5: Subplots of relative errors versus injected parameters for ECC detector with **SLy EoS**

4.2 BNS results

The runs used to generate the above results have been done by Ish Gupta on the LIGO cluster. The results show consistency with the values that we have injected. As predicted the accuracy of the **ECC** detector is more in these cases. The generated runs for this model correspond to the low mass system. Therefore, in these runs, we have kept both the tidal deformability as free parameters and hence we can see that the **IMRPhenomTidalv2** is an appropriate waveform approximant for the low mass system runs.

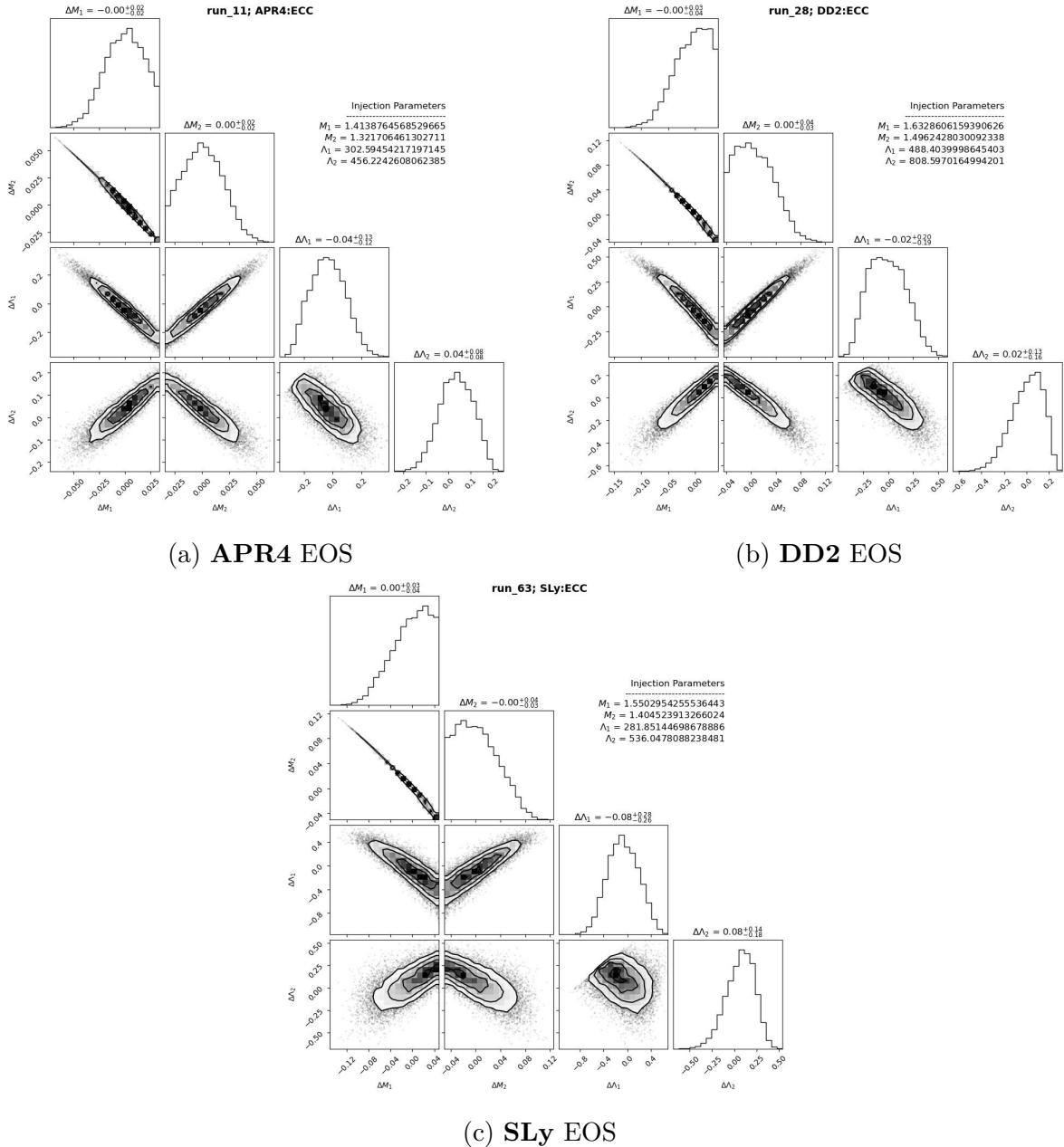


Figure 4.6: Corner plots of best runs for BNS for ECC detectors using **IMRPhenomTidalv2** waveform approximant for APR4, DD2 and SLy EOS

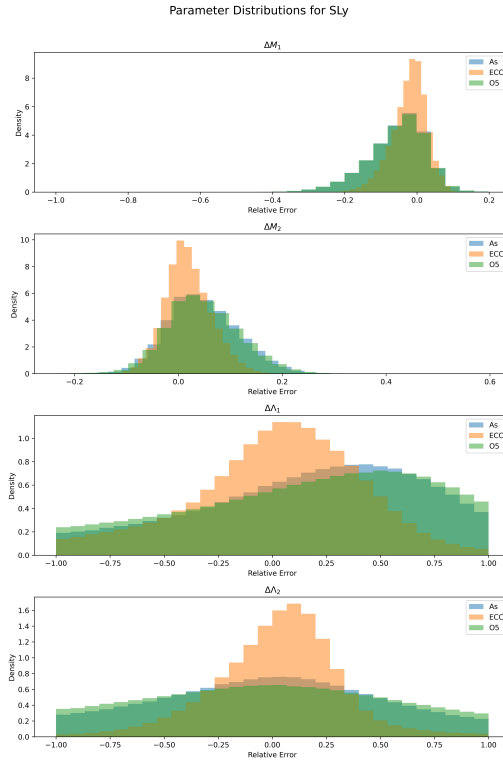
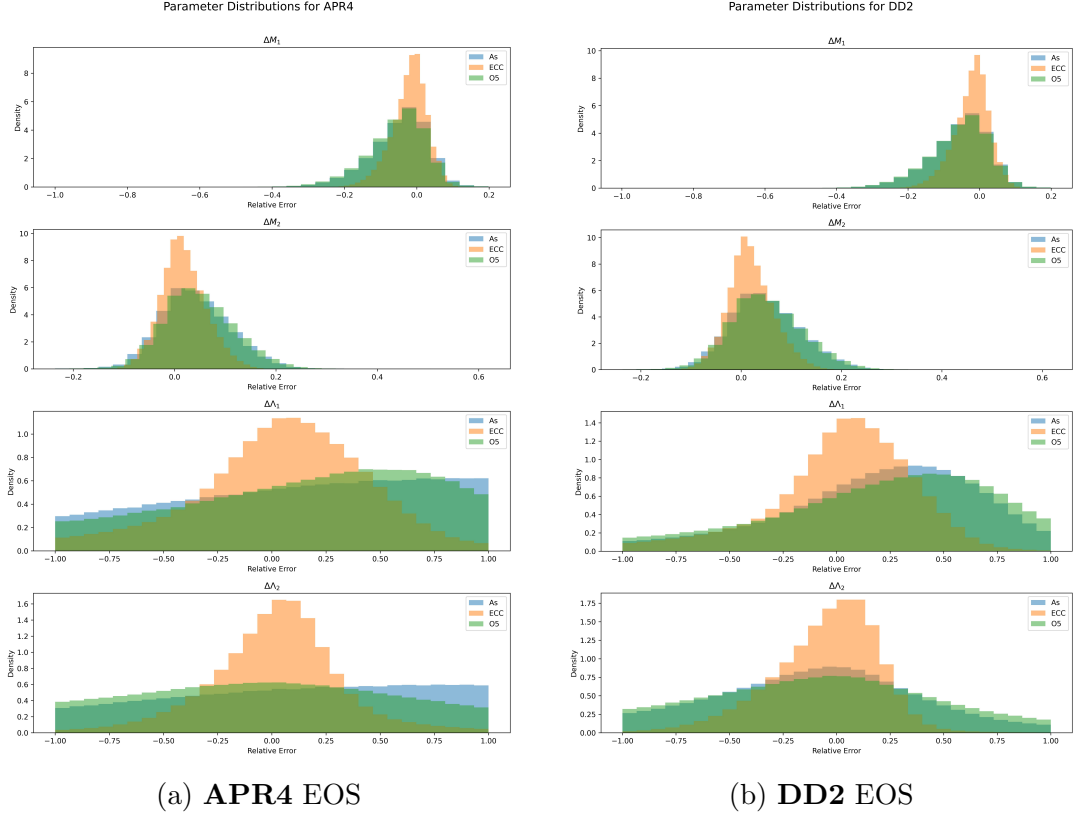


Figure 4.7: Comparisons between relative errors in 4 parameters among 100 BNS runs for 3 detectors using **IMRPhenomTidalv2** waveform approximant for **APR4**, **DD2** and **SLy EOS**

4.3 Calculated Lightcurves

4.3.1 Filters used:

We have used 4 filters in Optically visible band and 3 filters in Infrared regions. These filters are from the the SVO Filter Profile Service "Carlos Rodrigo", funded by MCIN/AEI/10.13039/50110

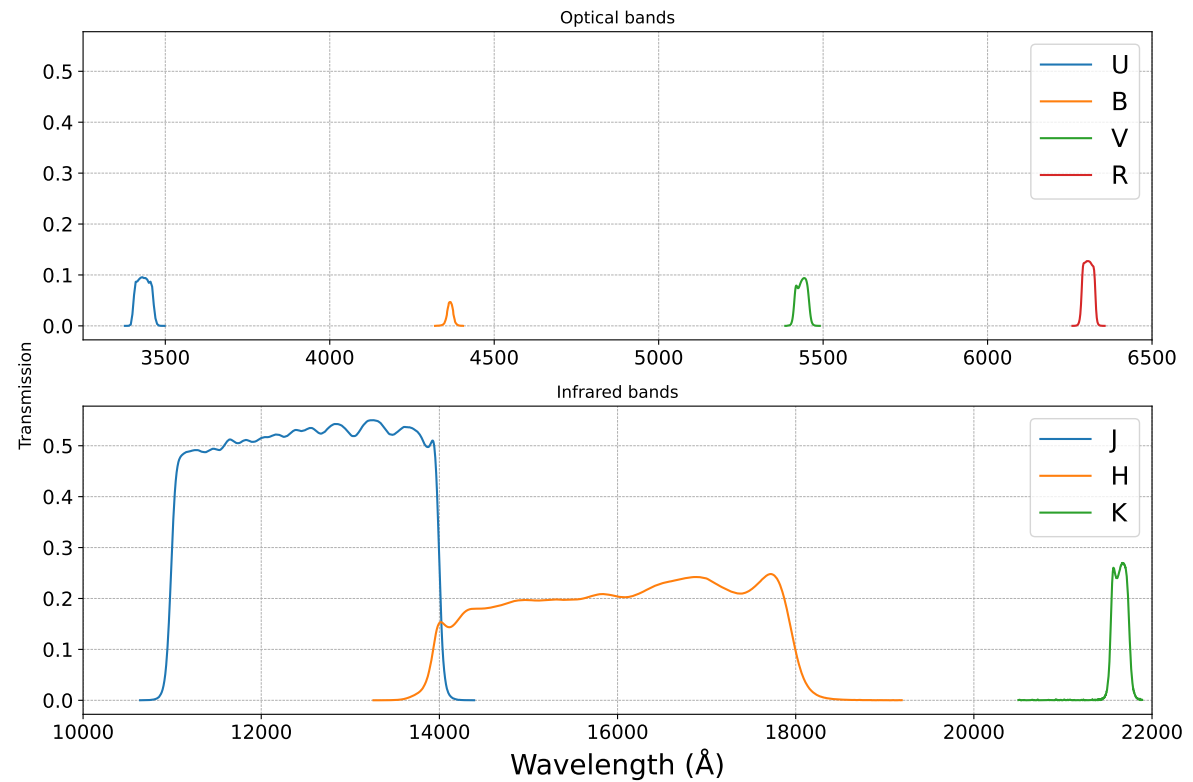


Figure 4.8: *Filter transmission as function of wavelength*

4.3.2 For NSBH system:

The bandwise light curve generated from our mapping function/methods is similar to what we observed. It peaks faster and also decays faster in the optical band. The comparison between realistic filters, characterised by their wavelength range distribution, and ideal filters, represented by the Dirac delta function, indicates that realistic filters closely approximate ideal filters.

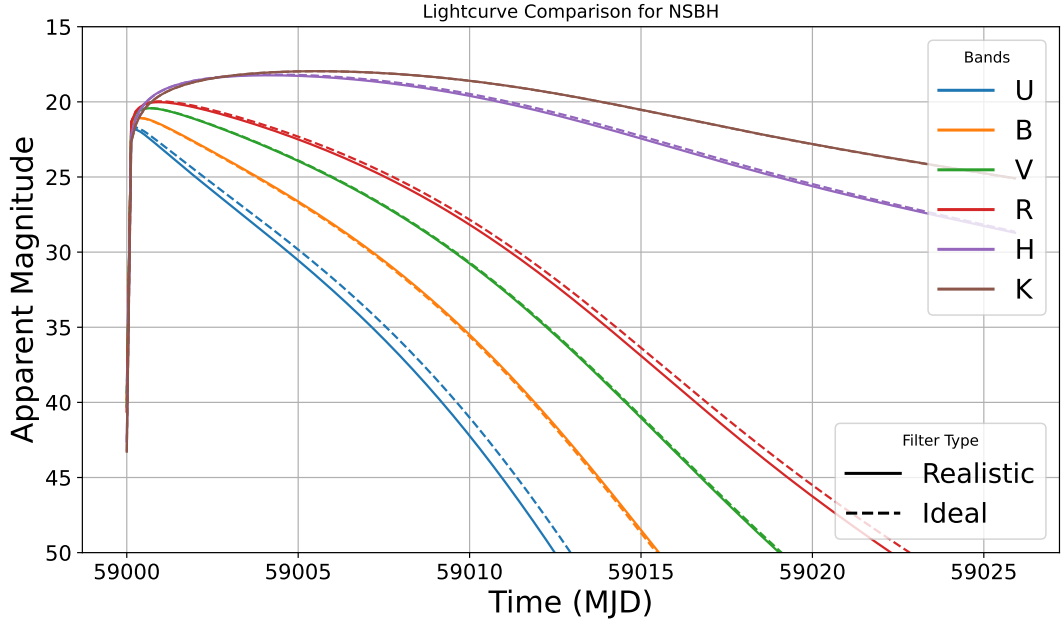


Figure 4.9: *Comparison between Apparent Magnitude bandwise lightcurves using realistic and ideal filters for NSBH system*

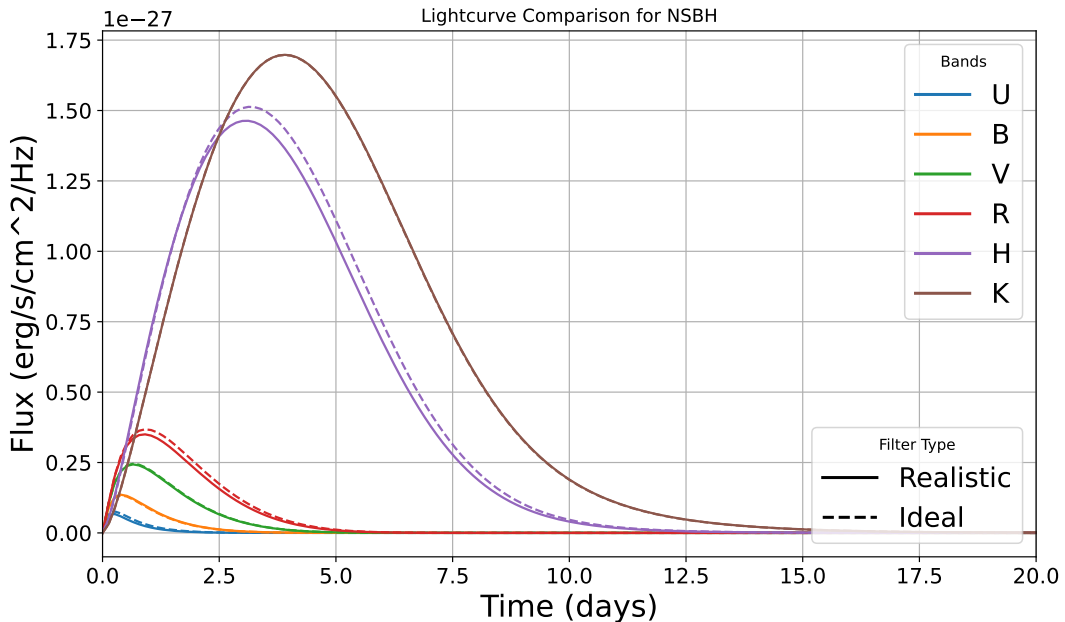


Figure 4.10: *Comparison between bandwise lightcurves using realistic and ideal filters*

For parameter estimation using MOSFiT, we have injected the following parameters from our NSBH lightcurve model,

Parameters	Injected value
Λ_{eff}	22.62
M_{chirp}	$1.83M_\odot$
χ_{BH}	0.15
q	0.27

Table 4.2: Injected parameter

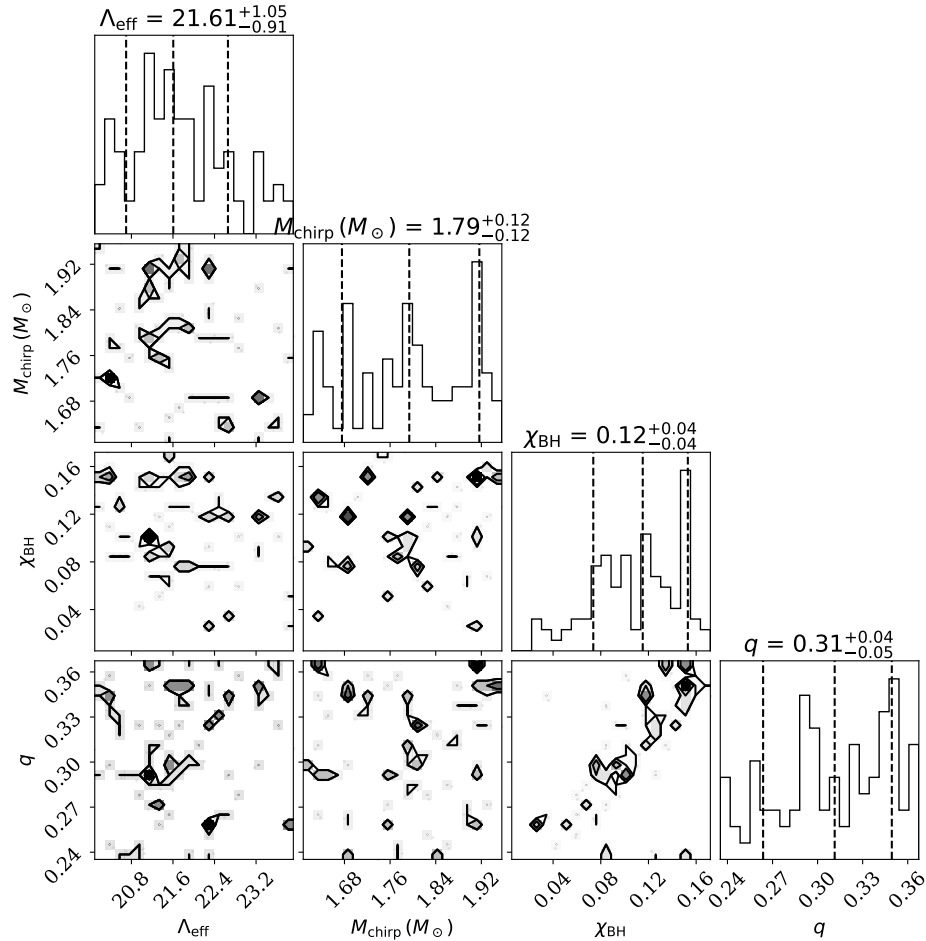


Figure 4.11: Corner plot for parameter estimation using MOSFiT's NSBH model

From the following figure, it's quite evident that we have recovered all the injected parameters within the $\pm 1\sigma$

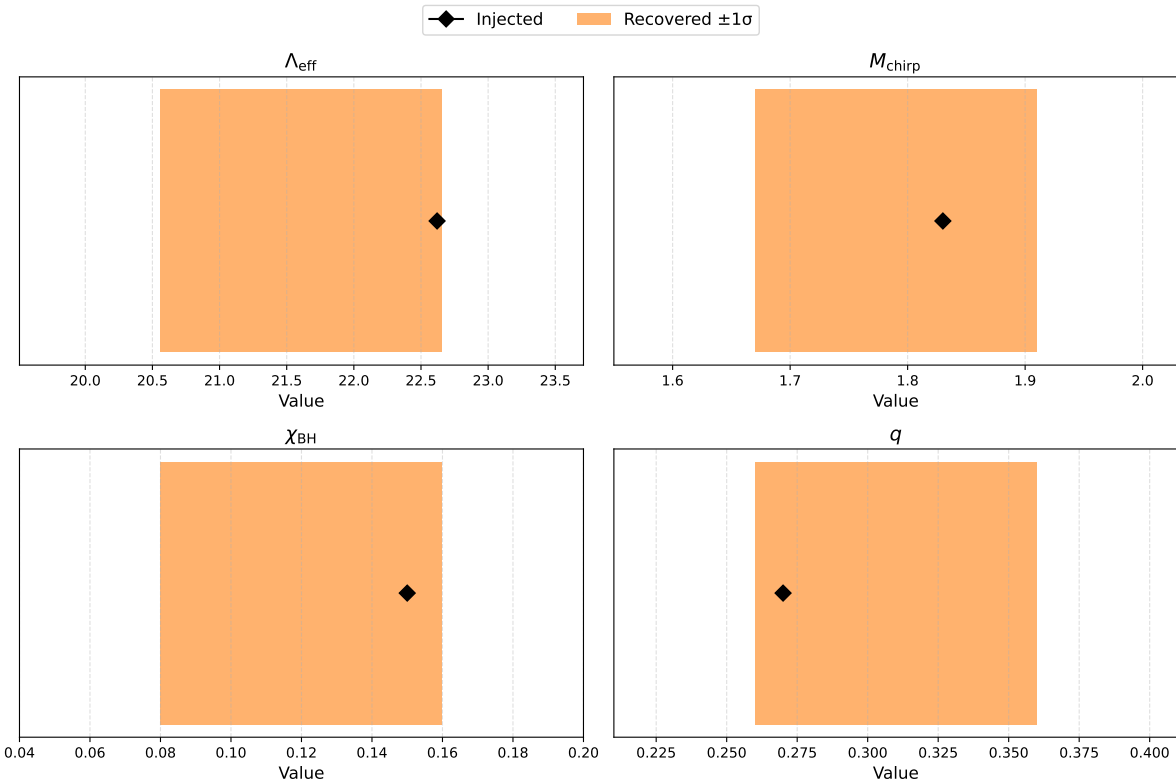


Figure 4.12: *A bullet plot showing comparison between injected and recovered parameters for NSBH system*

4.3.3 For BNS system:

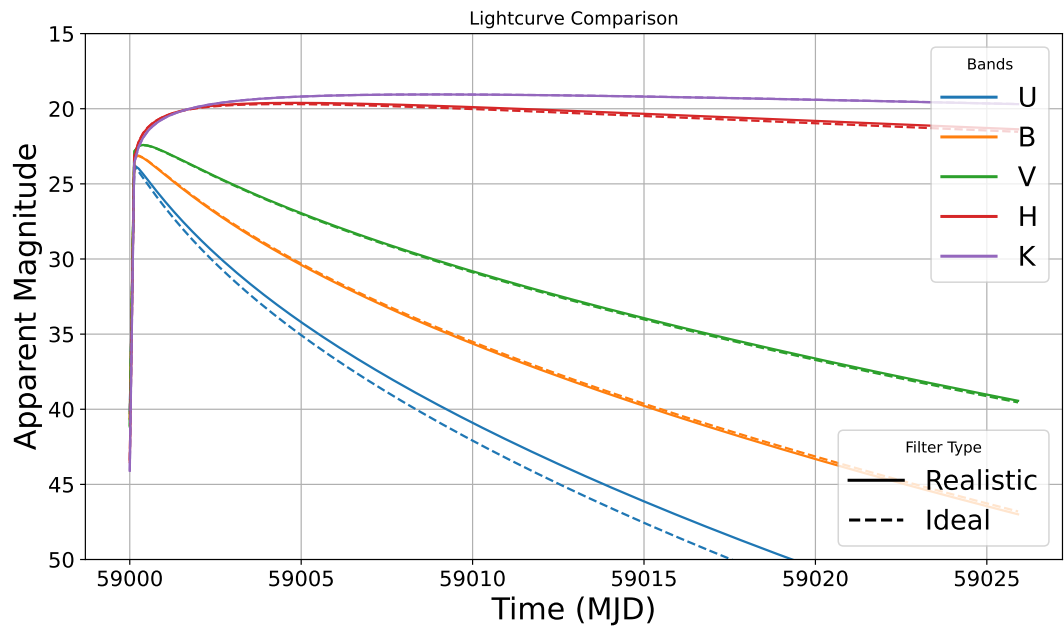


Figure 4.13: *Comparison between **Apparent Magnitude** bandwise lightcurves using realistic and ideal filters for BNS system*

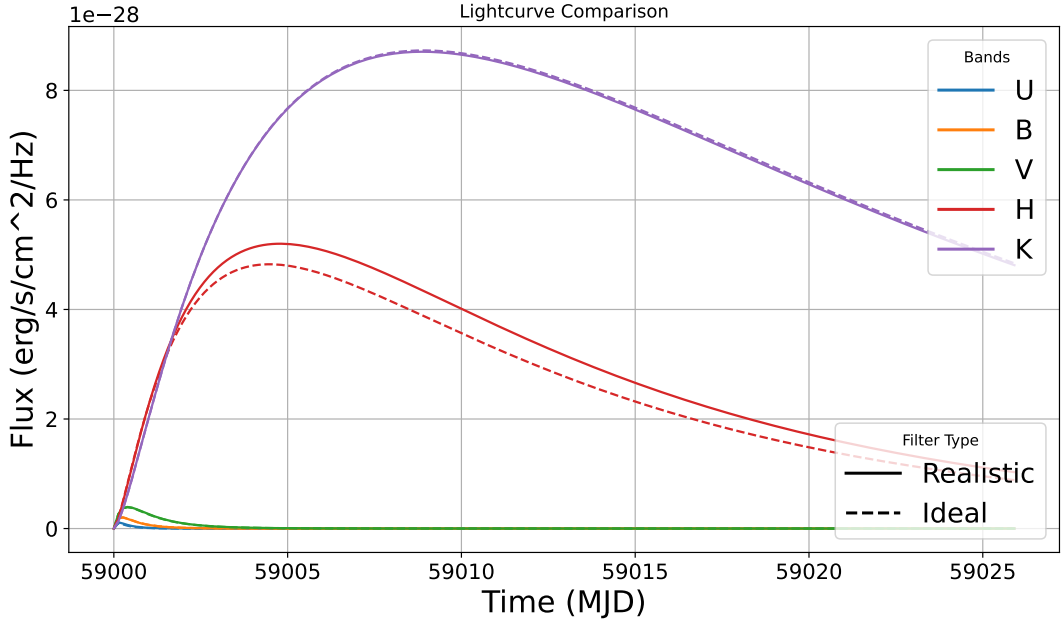


Figure 4.14: *Comparison between bandwise lightcurves using **realistic** and **ideal** filters*

[h!] For parameter estimation using MOSFiT, we have injected the following parameters from our BNS lightcurve model,

Parametrs	Injected value
Λ_s	18
M_{chirp}	$1.90M_\odot$
M_{TOV}	2.30
q	0.995

Table 4.3: **Injected parameter**

From the following figure, it's quite evident that we have recovered all the injected parameters within the $\pm 1\sigma$

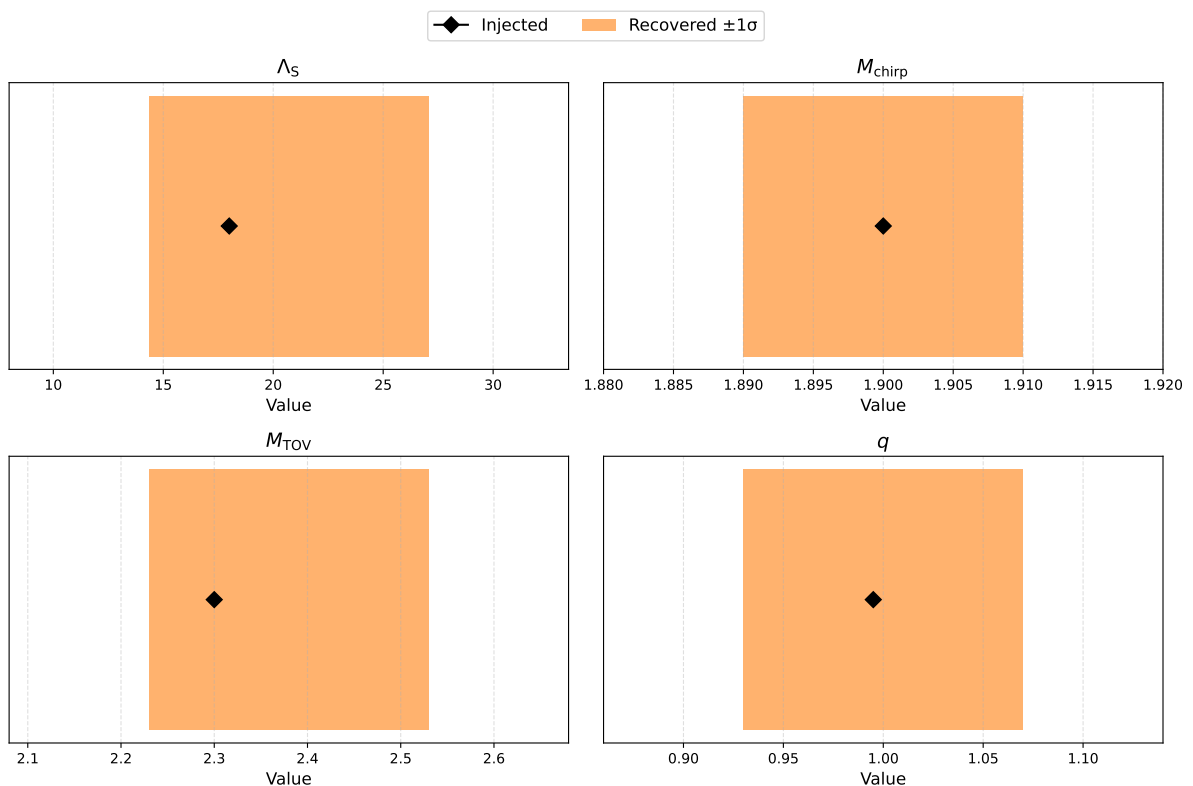


Figure 4.15: A bullet plot showing comparison between injected and recovered parameters for BNS system

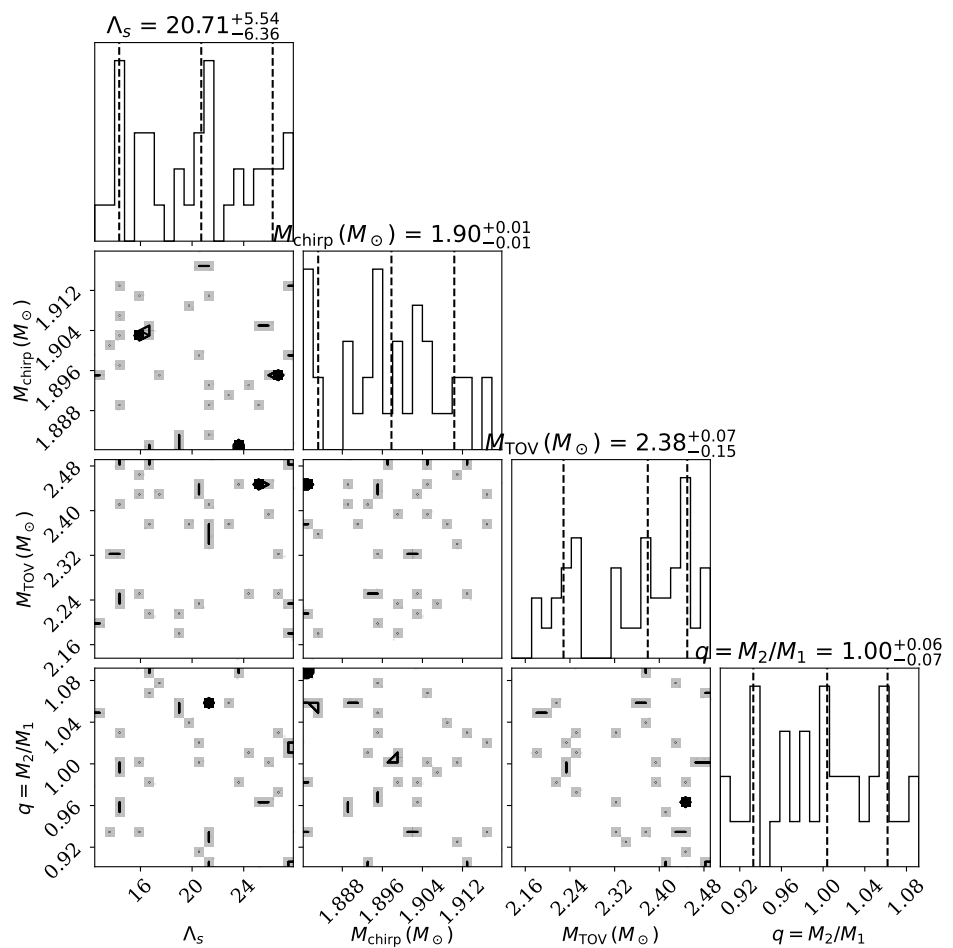


Figure 4.16: Corner plot for parameter estimation using MOSFiT's BNS model

Chapter 5

Future Work

Up until now the work on **Bilby** pipeline is completed. Some of the modifications on MOSFiT have also been done. In the next upcoming semester will try to produce more accurate results by fixing the tidal deformability of heavier companion to zero i.e. $\Lambda_1 = 0$ and using **IMRPhenomNSBH** approximant to for higher mass systems (generally for $M_1 > 5M_\odot$). And for low mass system (generally $1.2M_\odot < M_1 < 5M_\odot$) we will keep both tidal deformability to be a free parameter while using **IMRPhenomTidalv2** as waveform approximant. Following this we will proceed with the **Bayes factor** calculation. Inside of the **MOSFiT**'s modification the inclusion of parameter estimation on M_{NS} , M_{BH} , χ_{BH} and Λ_{NS} is still pending. This will help to perform the light curve analysis which is very crucial to this project. Furthermore, the NSBH runs which are currently running on IIT Bombay's Spacetime cluster are taking too much computational time and resources to generate the results. So, the next task in this direction is to reduce the computational cost by optimizing and parallelizing the code.

Chapter 6

Conclusion

Up to this point, the analysis has demonstrated that the **IMRPhenomTidalv2** waveform approximant is more effective for parameter estimation using Bayesian methods for lower mass systems (typically with $1.2M_{\odot} < M_1 < 5M_{\odot}$) where both tidal deformabilities are non-zero, more aligning with BNS models. Conversely, for higher mass systems (generally when $M_1 > 5M_{\odot}$), where one tidal deformability is zero (typical of NSBH models), the **IMRPhenomNSBH** waveform approximant has proven to yield more precise results. This distinction is critical for ensuring accurate parameter recovery and efficient model selection across different merger scenarios. From Lightcurve perspective, Matt Nichol's model is in close resemblance to that of an actual observed KN lightcurve. Matt Nichol's has worked on GW170817, while we are working on a population of mergers to distinguish the type of merger based on bayes factor favourism. Also, as we have seen from the bullet plots from result section 4.12 and 4.15 that the model that we are using for NSBH and BNS are consistent with the observed/simulated data.

Bibliography

- [1] W. D. Arnett. Analytic solutions for light curves of supernovae of Type II. , 237: 541–549, April 1980. doi: 10.1086/157898.
- [2] W. D. Arnett. Type I supernovae. I - Analytic solutions for the early part of the light curve. , 253:785–797, February 1982. doi: 10.1086/159681.
- [3] Gregory Ashton et al. BILBY: A user-friendly Bayesian inference library for gravitational-wave astronomy. *Astrophys. J. Suppl.*, 241(2):27, 2019. doi: 10.3847/1538-4365/ab06fc.
- [4] C. Barbieri, O. S. Salafia, A. Perego, M. Colpi, and G. Ghirlanda. Light-curve models of black hole – neutron star mergers: steps towards a multi-messenger parameter estimation. *Astronomy amp; Astrophysics*, 625:A152, May 2019. ISSN 1432-0746. doi: 10.1051/0004-6361/201935443. URL <http://dx.doi.org/10.1051/0004-6361/201935443>.
- [5] Jennifer Barnes, Daniel Kasen, Meng-Ru Wu, and Gabriel Martínez-Pinedo. Radioactivity and thermalization in the ejecta of compact object mergers and their impact on kilonova light curves. *The Astrophysical Journal*, 829(2):110, September 2016. ISSN 1538-4357. doi: 10.3847/0004-637x/829/2/110. URL <http://dx.doi.org/10.3847/0004-637X/829/2/110>.
- [6] E. Berger, W. Fong, and R. Chornock. An r-process kilonova associated with the short-hard grb 130603b. *The Astrophysical Journal*, 774(2), 2013. ISSN 2041-8213. doi: 10.1088/2041-8205/774/2/l23. URL <http://dx.doi.org/10.1088/2041-8205/774/2/L23>.
- [7] Oliver M. Boersma and Joeri van Leeuwen. Investigating the detection rates and inference of gravitational-wave and radio emission from black hole neutron star mergers. *Astronomy amp; Astrophysics*, 664:A160, August 2022. ISSN 1432-0746. doi: 10.1051/0004-6361/202243267. URL <http://dx.doi.org/10.1051/0004-6361/202243267>.
- [8] Tim Dietrich and Maximiliano Ujevic. Modeling dynamical ejecta from binary neutron star mergers and implications for electromagnetic counterparts. *Classical and Quantum Gravity*, 34(10):105014, April 2017. ISSN 1361-6382. doi: 10.1088/1361-6382/aa6bb0. URL <http://dx.doi.org/10.1088/1361-6382/aa6bb0>.
- [9] Nick Ekanger, Mukul Bhattacharya, and Shunsaku Horiuchi. Nucleosynthesis in outflows of compact objects and detection prospects of associated kilonovae. *Monthly Notices of the Royal Astronomical Society*, 525(2):2040–2052, August 2023. ISSN

1365-2966. doi: 10.1093/mnras/stad2348. URL <http://dx.doi.org/10.1093/mnras/stad2348>.

- [10] Abbott et. al. Multi-messenger observations of a binary neutron star merger*. *The Astrophysical Journal Letters*, 848(2), 2017. ISSN 2041-8213. doi: 10.3847/2041-8213/aa91c9. URL <http://dx.doi.org/10.3847/2041-8213/aa91c9>.
- [11] Abbott et.al. Observation of gravitational waves from a binary black hole merger. *Physical Review Letters*, 116(6), February 2016. ISSN 1079-7114. doi: 10.1103/physrevlett.116.061102. URL <http://dx.doi.org/10.1103/PhysRevLett.116.061102>.
- [12] Sho Fujibayashi, Kenta Kiuchi, Shinya Wanajo, Koutarou Kyutoku, Yuichiro Sekiguchi, and Masaru Shibata. Comprehensive study of mass ejection and nucleosynthesis in binary neutron star mergers leaving short-lived massive neutron stars. *The Astrophysical Journal*, 942(1):39, January 2023. ISSN 1538-4357. doi: 10.3847/1538-4357/ac9ce0. URL <http://dx.doi.org/10.3847/1538-4357/ac9ce0>.
- [13] Jonathan Gair. Making sense of data: Introduction to statistics for gravitational wave astronomy, November 2019.
- [14] J. H. Gillanders and S. J. Smartt. Analysis of the jwst spectra of the kilonova accompanying grb 230307a, 2024. URL <https://arxiv.org/abs/2408.11093>.
- [15] J. Guillochon, M. Nicholl, V. A. Villar, B. Mockler, G. Narayan, K. S. Mandel, E. Berger, and P. K. G. Williams. MOSFiT: Modular Open-Source Fitter for Transients. *ArXiv e-prints*, October 2017.
- [16] Erika M. Holmbeck, Jennifer Barnes, Kelsey A. Lund, Trevor M. Sprouse, G. C. McLaughlin, and Matthew R. Mumpower. Superheavy elements in kilonovae. *The Astrophysical Journal Letters*, 951(1):L13, June 2023. ISSN 2041-8213. doi: 10.3847/2041-8213/acd9cb. URL <http://dx.doi.org/10.3847/2041-8213/acd9cb>.
- [17] K. et al. Hotokezaka. Radioactive decay products in neutron star merger ejecta: heating efficiency and -ray emission. *Monthly Notices of the Royal Astronomical Society*, 459(1):35–43, 04 2016. ISSN 0035-8711. doi: 10.1093/mnras/stw404. URL <https://doi.org/10.1093/mnras/stw404>.
- [18] Kenta Hotokezaka, Re'em Sari, and Tsvi Piran. Analytic heating rate of neutron star merger ejecta derived from fermi's theory of beta decay. *Monthly Notices of the Royal Astronomical Society*, 468(1):91–96, February 2017. ISSN 1365-2966. doi: 10.1093/mnras/stx411. URL <http://dx.doi.org/10.1093/mnras/stx411>.
- [19] Rahul Kashyap, Gayathri Raman, and Parameswaran Ajith. Can kilonova light curves be standardized? *The Astrophysical Journal Letters*, 886(1):L19, November 2019. ISSN 2041-8213. doi: 10.3847/2041-8213/ab543f. URL <http://dx.doi.org/10.3847/2041-8213/ab543f>.
- [20] Rahul Kashyap, Arnab Dhani, and Bangalore Sathyaprakash. Systematic errors due to quasiuniversal relations in binary neutron stars and their correction for unbiased model selection. *Phys. Rev. D*, 106:123001, Dec 2022. doi: 10.1103/PhysRevD.106.123001. URL <https://link.aps.org/doi/10.1103/PhysRevD.106.123001>.

- [21] O. Korobkin, S. Rosswog, A. Arcones, and C. Winteler. On the astrophysical robustness of the neutron star merger r-process: Robust r-process in neutron star mergers. *Monthly Notices of the Royal Astronomical Society*, 426(3):1940–1949, October 2012. ISSN 0035-8711. doi: 10.1111/j.1365-2966.2012.21859.x. URL <http://dx.doi.org/10.1111/j.1365-2966.2012.21859.x>.
- [22] Li-Xin Li and Bohdan Paczyński. Transient events from neutron star mergers. *The Astrophysical Journal*, 507(1):L59–L62, November 1998. ISSN 0004-637X. doi: 10.1086/311680. URL <http://dx.doi.org/10.1086/311680>.
- [23] LIGO Scientific Collaboration, Virgo Collaboration, and KAGRA Collaboration. LVK Algorithm Library - LALSuite. Free software (GPL), 2018.
- [24] Brian D. Metzger. Kilonovae. *Living Reviews in Relativity*, 20(1), May 2017. ISSN 1433-8351. doi: 10.1007/s41114-017-0006-z. URL <http://dx.doi.org/10.1007/s41114-017-0006-z>.
- [25] Rajesh Kumble Nayak. Challenges in source parameter estimation in gw astronomy, March 2017.
- [26] Matt Nicholl, Ben Margalit, Patricia Schmidt, Graham P Smith, Evan J Ridley, and James Nuttall. Tight multimessenger constraints on the neutron star equation of state from gw170817 and a forward model for kilonova light-curve synthesis. *Monthly Notices of the Royal Astronomical Society*, 505(2):3016–3032, May 2021. ISSN 1365-2966. doi: 10.1093/mnras/stab1523. URL <http://dx.doi.org/10.1093/mnras/stab1523>.
- [27] David Radice, Albino Perego, Kenta Hotokezaka, Steven A. Fromm, Sebastiano Bernuzzi, and Luke F. Roberts. Binary neutron star mergers: Mass ejection, electromagnetic counterparts, and nucleosynthesis. *The Astrophysical Journal*, 869(2):130, December 2018. ISSN 1538-4357. doi: 10.3847/1538-4357/aaf054. URL <http://dx.doi.org/10.3847/1538-4357/aaf054>.
- [28] S. Rowan and J. Hough. The detection of gravitational waves. In *1998 European School of High-Energy Physics*, pages 301–311, 1998.
- [29] N. R. Tanvir, A. J. Levan, A. S. Fruchter, J. Hjorth, R. A. Hounsell, K. Wiersema, and R. L. Tunnicliffe. A ‘kilonova’ associated with the short-duration -ray burst grb130603b. *Nature*, 500(7464):547–549, August 2013. ISSN 1476-4687. doi: 10.1038/nature12505. URL <http://dx.doi.org/10.1038/nature12505>.
- [30] Eric Thrane and Colm Talbot. An introduction to bayesian inference in gravitational-wave astronomy: Parameter estimation, model selection, and hierarchical models. *Publications of the Astronomical Society of Australia*, 36, 2019. ISSN 1448-6083. doi: 10.1017/pasa.2019.2. URL <http://dx.doi.org/10.1017/pasa.2019.2>.
- [31] Andrew Toivonen, Gargi Mansingh, Holton Griffin, Armita Kazemi, Frank Kerkow, Stephen K. Mahanty, Jacob Markus, Seiya Tsukamoto, Sushant Sharma Chaudhary, Sarah Antier, Michael W. Coughlin, Deep Chatterjee, Reed Essick, Shaon Ghosh, Tim Dietrich, and Philippe Landry. What to expect: kilonova light curve predictions via equation of state marginalization, 2024. URL <https://arxiv.org/abs/2410.10702>.